

ARTICLE TYPE

Extended isogeometric analysis of a progressively fracturing fluid-saturated porous medium

Farshid Fathi | Lin Chen | Tim Hageman | René de Borst*

Department of Civil and Structural
Engineering, University of Sheffield,
Sheffield, UK

Correspondence

*Department of Civil and Structural
Engineering, University of Sheffield,
Sheffield, S1 3JD, UK
Email: r.deborst@sheffield.ac.uk

ABSTRACT

An extended isogeometric analysis (XIGA) approach is proposed for modelling fracturing in a fluid-saturated porous material. XIGA provides a definition of the discontinuity independent of the underlying mesh layout, which obviates the need of knowing the crack extension direction a priori. Unlike Lagrange shape functions used in the standard finite element approach, Non-Uniform Rational B-Splines (NURBS) provide a higher-order interelement continuity which leads to a continuous fluid flow also at element boundaries, thereby satisfying the local mass balance. It also leads to an improved estimate of the crack path due to a smoother stress distribution. The NURBS basis functions are cast in finite element data structure using Bézier extraction. To model the discontinuity, the Heaviside sign function is utilised within the displacement and the pressure fields, complemented by the shifting and the blending techniques to enforce compatibility perpendicular and parallel to the crack path, respectively. Different aspects of the approach are assessed through examples comprising straight and curved crack paths for stationary and propagating discontinuities.

KEYWORDS:

Extended finite element method, isogeometric analysis, porous material, fluid flow, cohesive fracture

1 | INTRODUCTION

Fluid flow in a deforming porous medium is a topic of major attention due to its numerous applications in, for instance, petroleum and geotechnical engineering^{1,2}, biology and medical sciences^{3,4,5}, and three or four-phase media^{6,7,8}. Initially, the theory was limited to intact porous materials^{9,10,11,12}. Analytical solutions which include fractures are available^{13,14,15}, but are subject to simplifying assumptions such as linear elasticity, homogeneity and impermeability, as well as idealised geometries. One of the earliest numerical models which considered a discontinuity, including fluid flow in the surrounding porous medium was proposed by Boone and Ingraffea¹⁶, exploiting a combination of finite element and finite difference methods.

The advent of interface elements paved the way for modelling discontinuities embedded in an otherwise continuous medium. They have become popular owing to their simple implementation and robust computational performance^{17,18,19,20,21}. A disadvantage of interface elements is that they require an a priori knowledge of the crack extension direction. Remeshing was introduced as the remedy for the arbitrary crack propagation^{22,23,24}, also in saturated porous media^{25,26}.

A more elegant approach to arbitrary crack paths is the extended finite element method (XFEM), where the crack path is decoupled from the underlying mesh layout. It was first developed for linear elastic fracture mechanics (LEFM)^{27,28} and subsequently developed for cohesive fracture^{29,30,31}. Different aspects of XFEM within saturated/unsaturated porous media have been

studied^{32,33,34}, including shear banding³⁵ and large deformation³⁶. Moreover, the implications of assuming a continuous or a discontinuous pressure across the discontinuity have been assessed³⁷. Embedded Strong Discontinuity Finite Element Method (ESD-FEM) is the other option to simulate the propagation of strain localisation in porous media^{38,39,40}.

In (un)saturated porous media standard finite element analysis typically does not locally conserve mass owing to the C^0 -continuity at element boundaries. Lagrange basis functions lead to a discontinuous interelement pressure gradient and therefore to a loss of local mass balance, unless special degrees of freedom are used⁴¹. Meshfree methods have been exploited to resolve this issue as they provide a higher order of continuity, and consequently, a smoother stress field and pressure gradient^{42,43,44}. Nevertheless, a higher computational cost compared to finite element methods and the poor geometric parametrisation of the complex boundaries are disadvantages of meshfree approaches, which have limited their use.

A more promising alternative to provide higher-order continuity is isogeometric analysis (IGA), originally proposed to connect the design and the analysis tools in order to obtain the highest possible precision in geometric parametrisation and to reduce the computational cost through bypassing the mesh generation stage^{45,46,47}. For poroelasticity IGA was first adopted for the intact porous materials⁴⁸, and developed subsequently for fractured and/or fracturing porous media using hydromechanical interface elements^{20,21,49,50,51}. Later, the extension was made to the simulation of non-Newtonian fluids and multi-phase flows^{52,53,54,55}. Moreover, other isogeometric applications, namely collocation methods⁵⁶, are studied for poromechanics problems.

De Luycker et al.⁵⁷ were first to develop an extended isogeometric approach (XIGA), blending concepts of XFEM and IGA. This is possible owing to the fact that B-spline and NURBS basis functions form a partition of unity, which is necessary to define extra layers of approximants. Unlike the original work, compatibility enforcement was absent in later XIGA contributions^{58,59}, which is, however, necessary to render the original and the extra layers consistent. This is of utmost importance, particularly for XIGA, where higher interelement continuity at the element boundaries extends the discontinuous domain to the intact zones, but then in an incorrect manner. For this reason compatibility enforcement was studied comprehensively when trying to develop XIGA for cohesive fracture⁶⁰. The consequences of an incomplete enforcement were also observed in a study on geometric nonlinearity⁶¹. More recently, IGA was extended with a local maximum entropy (LME), coined X-IGALME⁶², in order to blend finite element and meshfree methods. This approach yields some outstanding features, in particular the singularity-free property of X-IGALME regardless of the crack location within the mesh, which is a major issue in element-based extended approaches⁶³.

Herein, we adopt XIGA to model fracturing in a fully saturated porous media. Rate-independent, isotropic linear elasticity is used for the solid skeleton, and a cohesive-zone model governs at the crack propagation. A small displacement gradient is assumed throughout. Poroelasticity is considered for the interstitial fluid, while a discontinuous pressure (two degrees of freedom) model defines the fluid behaviour at the discontinuity^{32,19}. A two pressure degrees of freedom (2PDOF) model enables fluid flow perpendicular to the crack as fluid pressure values can be different at both sides of the crack. It also allows for the use of Heaviside sign function for both displacement and pressure fields, leading to a compatibility enforcement similar to that of the solid phase. Indeed, there is no need for a micro-flow model within the fracture, which allows for the simplest approach with minimal requirements. Nevertheless, since in a 2PDOF model the fluid pressure is absent inside the fracture, 1PDOF and 3PDOF models are superior to a 2PDOF model for hydraulic fracturing problems. Non-Uniform Rational B-Splines (NURBS) are adopted for the discretisation. They are cast within a standard finite element data structure using Bézier extraction^{64,20}.

We first briefly summarise the governing equations for the poromechanical problem, including the governing relations at the discontinuity. They are linearised and discretised using Bézier extraction-based NURBS and incorporated in a standard finite element matrix notation. Next, implementation aspects are covered, encompassing compatibility, enrichment, integration and crack extension. The contribution concludes with case studies which demonstrate the capability of the proposed approach in modelling a stationary fracture, followed by a study of a progressively fracturing porous medium, comprising straight and curved crack paths.

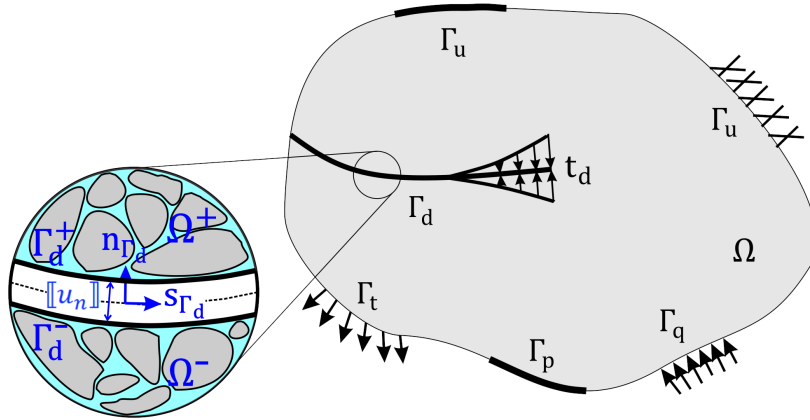


FIGURE 1 Boundary value problem Ω with the discontinuity Γ_d and cohesive tractions \mathbf{t}_d .

2 | MECHANICAL PROBLEM

We consider a fully saturated porous body Ω , which contains a discontinuity Γ_d , see Figure 1. In the absence of the acceleration and body forces, the quasi-static equilibrium equation reads:

$$\begin{cases} \nabla \cdot \boldsymbol{\sigma} = 0 & \mathbf{x} \in \Omega \\ \mathbf{u} = \bar{\mathbf{u}} & \mathbf{x} \in \Gamma_u \\ \mathbf{n}_t \cdot \boldsymbol{\sigma} = \bar{\mathbf{t}} & \mathbf{x} \in \Gamma_t \\ \mathbf{n}_{\Gamma_d} \cdot \boldsymbol{\sigma} = \mathbf{t}_d & \mathbf{x} \in \Gamma_d \end{cases} \quad (1)$$

where $\boldsymbol{\sigma}$ is the Cauchy stress tensor, \mathbf{n}_{Γ_d} and \mathbf{n}_t are the vectors normal to the fracture and the external traction surface Γ_t , respectively. The prescribed values for displacements and tractions are referred to as $\bar{\mathbf{u}}$ and $\bar{\mathbf{t}}$, respectively. The discontinuity is imposed within the displacement field with a Heaviside function $\mathbf{n}_{\Gamma_d} \cdot \nabla D_{\Gamma_d} = \mathcal{H}_{\Gamma_d}$, where D_{Γ_d} is the sign distance function, leading to $\mathbf{u} = \hat{\mathbf{u}} + \mathcal{H}_{\Gamma_d} \tilde{\mathbf{u}}$ which is comprised of continuous (standard) $\hat{\mathbf{u}}$ and discontinuous (enhanced) $\tilde{\mathbf{u}}$ parts⁶⁰.

Recalling the small displacement assumption and its gradient, the infinitesimal strain field becomes:

$$\boldsymbol{\epsilon} = \nabla \hat{\mathbf{u}} + \mathcal{H}_{\Gamma_d} \nabla \tilde{\mathbf{u}} + 2\delta_{\Gamma_d} (\tilde{\mathbf{u}} \otimes \mathbf{n}_{\Gamma_d}) \quad (2)$$

where δ_{Γ_d} is the Dirac-delta and follows the identity $\mathbf{n}_{\Gamma_d} \cdot \nabla \mathcal{H}_{\Gamma_d} = 2\delta_{\Gamma_d}$. The constitutive law for the solid part yields:

$$\boldsymbol{\sigma}_s = \mathbf{D} : \boldsymbol{\epsilon} \quad (3)$$

where \mathbf{D} is the fourth-order linear-elastic stiffness tensor. Accordingly, the total stress tensor used in Equation (1) reads:

$$\boldsymbol{\sigma} = \boldsymbol{\sigma}_s - \alpha p \mathbf{1}. \quad (4)$$

α and p are the Biot coefficient and the pore fluid pressure, respectively. $\mathbf{1}$ indicates the identity matrix.

2.1 | Governing weak forms

Now, we write the weak form of Equation (1) to set the scene for the discretisation:

$$\int_{\Omega} \nabla \delta \mathbf{u} : \boldsymbol{\sigma} \, d\Omega + \int_{\Gamma_d} \delta [\![\mathbf{u}]\!] \cdot (\mathbf{n}_{\Gamma_d} \cdot \boldsymbol{\sigma}) \, d\Gamma = \int_{\Gamma_t} \delta \mathbf{u} \cdot \bar{\mathbf{t}} \, d\Gamma. \quad (5)$$

Inserting the displacement jump $[\![\mathbf{u}]\!] = \mathbf{u}^+ - \mathbf{u}^-$ into Equation 5 and defining a test function for the displacement field, $\delta \mathbf{u} = \delta \hat{\mathbf{u}} + \mathcal{H}_{\Gamma_d} \delta \tilde{\mathbf{u}}$, yields:

$$\int_{\Omega} \nabla \delta \mathbf{u} : \boldsymbol{\sigma} \, d\Omega + 2 \int_{\Gamma_d} \delta \tilde{\mathbf{u}} \cdot (\mathbf{n}_{\Gamma_d} \cdot \boldsymbol{\sigma}) \, d\Gamma = \int_{\Gamma_t} \delta \mathbf{u} \cdot \bar{\mathbf{t}} \, d\Gamma \quad (6)$$

where

$$\mathbf{n}_{\Gamma_d} \cdot \boldsymbol{\sigma} = \mathbf{t}_d - p \mathbf{n}_{\Gamma_d} \quad (7)$$

with t_d denoting the cohesive traction at the discontinuity. Equation (6) decomposes into two separate equations for $\delta \hat{\mathbf{u}}$ and $\delta \tilde{\mathbf{u}}$,

$$\int_{\Omega} \nabla \delta \hat{\mathbf{u}} : \boldsymbol{\sigma} \, d\Omega = \int_{\Gamma_i} \delta \hat{\mathbf{u}} \cdot \bar{\mathbf{t}} \, d\Gamma \quad (8a)$$

$$\int_{\Omega} \mathcal{H}_{\Gamma_d} \nabla \delta \tilde{\mathbf{u}} : \boldsymbol{\sigma} \, d\Omega + 2 \int_{\Gamma_d} \delta \tilde{\mathbf{u}} \cdot (\mathbf{n}_{\Gamma_d} \cdot \boldsymbol{\sigma}) \, d\Gamma = \int_{\Gamma_i} \mathcal{H}_{\Gamma_d} \delta \tilde{\mathbf{u}} \cdot \bar{\mathbf{t}} \, d\Gamma \quad (8b)$$

2.2 | Traction-separation relationship at the discontinuity

We use an exponential decay for the traction-relative opening relation at the discontinuity:

$$\mathbf{t}_d^{\text{loc}} = \mathbf{t}_d^{\text{loc}}(\llbracket \mathbf{u} \rrbracket, \kappa), \quad t_n^{\text{loc}} = f_t \exp\left(-\frac{f_t}{G_f} \kappa\right) \quad (9)$$

with the fracture energy and the tensile strength indicated by G_f and f_t , respectively. The history variable κ determines the loading/unloading condition by utilising Kuhn-Tucker conditions,

$$f(\llbracket u_n \rrbracket, \kappa) = \llbracket u_n \rrbracket - \kappa \leq 0 \quad \dot{\kappa} \geq 0 \quad \dot{\kappa} f = 0 \quad (10)$$

where $\llbracket u_n \rrbracket$ is the displacement jump normal to the crack. The shear stiffness is neglected in a pure mode-I fracture. To linearise the traction-separation relationship for a Newton-Raphson iterative scheme, it is transformed from the local to the global coordinate system using the rotation matrix \mathbf{Q} :

$$\mathbf{t}_d = \mathbf{Q}^T \mathbf{t}_d^{\text{loc}}. \quad (11)$$

3 | POROMECHANICAL PROBLEM

Next, the mass balance of an isotropic fully saturated porous medium is stated to complement the momentum balance given in Section 2. The interstitial fluid pressure can be computed from the mass conservation of the mixture:

$$\left\{ \begin{array}{ll} \alpha \nabla \cdot \dot{\mathbf{u}} + \nabla \cdot \mathbf{q} + \frac{1}{M} \dot{p} = 0 & \mathbf{x} \in \Omega \\ p = \bar{p} & \mathbf{x} \in \Gamma_p \\ \mathbf{n}_q \cdot \mathbf{q} = \bar{q} & \mathbf{x} \in \Gamma_q \\ \mathbf{n}_{\Gamma_d} \cdot \mathbf{q} = q_d & \mathbf{x} \in \Gamma_d \end{array} \right. \quad (12)$$

where M is the Biot modulus:

$$\frac{1}{M} = \frac{\alpha - n_f}{K_s} + \frac{n_f}{K_f} \quad (13)$$

with n_f the porosity of the medium, and K_s and K_f the solid and fluid bulk moduli, respectively.

The prescribed pressure and fluid flux are indicated by \bar{p} and \bar{q} , respectively. \mathbf{n}_q denotes the normal to the external flux surface. In this contribution we have chosen a discontinuous pressure field, i.e. $p = \hat{p} + \mathcal{H}_{\Gamma_d} \tilde{p}$, which leads to a discontinuous fluid flux:

$$\mathbf{q} = -k_f \nabla p = -k_f \left(\underbrace{\nabla \hat{p}}_{\text{continuous}} + \underbrace{\mathcal{H}_{\Gamma_d} \nabla \tilde{p} + 2\mathbf{n}_{\Gamma_d}^T \delta_{\Gamma_d} \tilde{p}}_{\text{discontinuous}} \right) \quad (14)$$

with k_f denoting the effective permeability, $k_f = k/\mu$. k and μ are the intrinsic permeability of the porous medium and the viscosity of the fluid, respectively. This is similar to a 2PDOF model of the fluid flow inside the fracture^{32,37}.

Since the fluid pressure and flux are assumed to be discontinuous across the discontinuity, the weak form reads:

$$-\int_{\Omega} \alpha \delta p \nabla \cdot \dot{\mathbf{u}} \, d\Omega - \int_{\Omega} k_f \nabla \delta p \nabla p \, d\Omega - \int_{\Omega} \delta p \frac{1}{M} \dot{p} \, d\Omega + \int_{\Gamma_d} \delta p \mathbf{n}_{\Gamma_d} \cdot \llbracket \mathbf{q}_d \rrbracket \, d\Gamma = \int_{\Gamma_q} \delta p \mathbf{n} \cdot \bar{\mathbf{q}} \, d\Gamma. \quad (15)$$

In the absence of an independent pressure degree of freedom inside the fracture, Equation (7) becomes:

$$\mathbf{n}_{\Gamma_d} \cdot \boldsymbol{\sigma} = t_d. \quad (16)$$

A 2PDOF model does not allow for the fluid flow along the fracture. Rather, the pressure jump is employed to directly compute the flux difference between the crack faces:

$$-\int_{\Omega} \alpha \delta p \nabla \cdot \dot{\mathbf{u}} \, d\Omega - \int_{\Omega} k_f \nabla \delta p \nabla p \, d\Omega - \int_{\Omega} \delta p \frac{1}{M} \dot{p} \, d\Omega - \int_{\Gamma_d} k_d \delta \tilde{p} \llbracket p_n \rrbracket \, d\Gamma = \int_{\Gamma_q} \delta p \mathbf{n} \cdot \bar{\mathbf{q}} \, d\Gamma \quad (17)$$

where k_d is the fracture permeability. It is noted that, based on the Heaviside sign function, the pressure jump becomes $\llbracket \mathbf{p} \rrbracket = \{\llbracket p_s \rrbracket, \llbracket p_n \rrbracket\} = (\mathcal{H}_{\Gamma_d}^+ - \mathcal{H}_{\Gamma_d}^-) \tilde{p} = 2\tilde{p}$. Equation (17) can be decomposed as:

$$-\int_{\Omega} \alpha \delta \tilde{p} \nabla \cdot \dot{\mathbf{u}} \, d\Omega - \int_{\Omega} k_f \nabla \delta \tilde{p} \nabla p \, d\Omega - \int_{\Omega} \delta \tilde{p} \frac{1}{M} \dot{p} \, d\Omega = \int_{\Gamma_q} \delta \tilde{p} \mathbf{n} \cdot \bar{\mathbf{q}} \, d\Gamma, \quad (18a)$$

$$-\int_{\Omega} \mathcal{H}_{\Gamma_d} \alpha \delta \tilde{p} \nabla \cdot \dot{\mathbf{u}} \, d\Omega - \int_{\Omega} \mathcal{H}_{\Gamma_d} k_f \nabla \delta \tilde{p} \nabla p \, d\Omega - \int_{\Omega} \mathcal{H}_{\Gamma_d} \frac{1}{M} \delta \tilde{p} \dot{p} \, d\Omega - 2 \int_{\Gamma_d} k_d \delta \tilde{p} \tilde{p} \, d\Gamma = \int_{\Gamma_q} \mathcal{H}_{\Gamma_d} \delta \tilde{p} \mathbf{n} \cdot \bar{\mathbf{q}} \, d\Gamma. \quad (18b)$$

4 | LINEARISED AND DISCRETISED EQUATIONS

4.1 | Bézier extraction based NURBS

A univariate B-spline basis function can be cast in terms of the Bézier extraction operator \mathbf{C} and a univariate Bernstein polynomial \mathbf{B} within the input domain $[-1 \, 1]$:

$$\mathbf{N}^e = \mathbf{C}^e \mathbf{B} \quad (19)$$

with

$$\mathcal{B}_{k,m}(\xi) = \frac{1}{2}(1 - \xi)\mathcal{B}_{k,m-1}(\xi) + \frac{1}{2}(1 + \xi)\mathcal{B}_{k-1,m-1}(\xi) \quad (20a)$$

$$\mathcal{B}_{1,0}(\xi) \equiv 1 \quad (20b)$$

$$\mathcal{B}_{k,m}(\xi) \equiv 0 \quad \text{if } k < 1 \text{ or } k > m + 1. \quad (20c)$$

where the superscript e indicates the element index and m denotes the order of the underlying knot vector. Making use of the tensor product a bivariate Bernstein polynomial results:

$$\mathcal{B}_{k,l}^{m,n}(\xi, \eta) = \mathcal{B}_{k,m}(\xi) \otimes \mathcal{B}_{l,n}(\eta). \quad (21)$$

Defining w_k as the weight of the corresponding knot and univariate B-spline basis functions N and M , the bivariate NURBS basis function reads^{64,65}:

$$R_{k,l}^{p,q}(\xi, \eta) = \frac{M_{l,q}(\eta) N_{k,p}(\xi) w_{k,l}}{\sum_{\hat{k}}^n \sum_{\hat{l}}^m M_{\hat{k},q}(\eta) N_{\hat{l},p}(\xi) w_{\hat{k},\hat{l}}}. \quad (22)$$

A NURBS surface is then rendered by:

$$\mathbf{S}(\xi, \eta) = \sum_{k=1}^n \sum_{l=1}^m R_{k,l}^{p,q}(\xi, \eta) \mathbf{p}_{k,l} \quad (23)$$

where \mathbf{p} is the set of control points in the physical domain. In the classical integration approach, two pull backs are required to compute the quadrature, see Figure 2. Compliance with the finite element data structure removes this restriction as the information on the parametric domain is preserved in the Bézier extraction operator \mathbf{C} .

4.2 | Discrete equations

We next discretise the velocity of the solid particles $\dot{\mathbf{u}}$ and the fluid pressure field p ,

$$\dot{\mathbf{u}} = \mathbf{R}_u (\dot{\hat{\mathbf{u}}} + \mathcal{H}_{\Gamma_d} \dot{\hat{\mathbf{u}}}), \quad p = \mathbf{R}_p (\hat{p} + \mathcal{H}_{\Gamma_d} \tilde{p}). \quad (24)$$

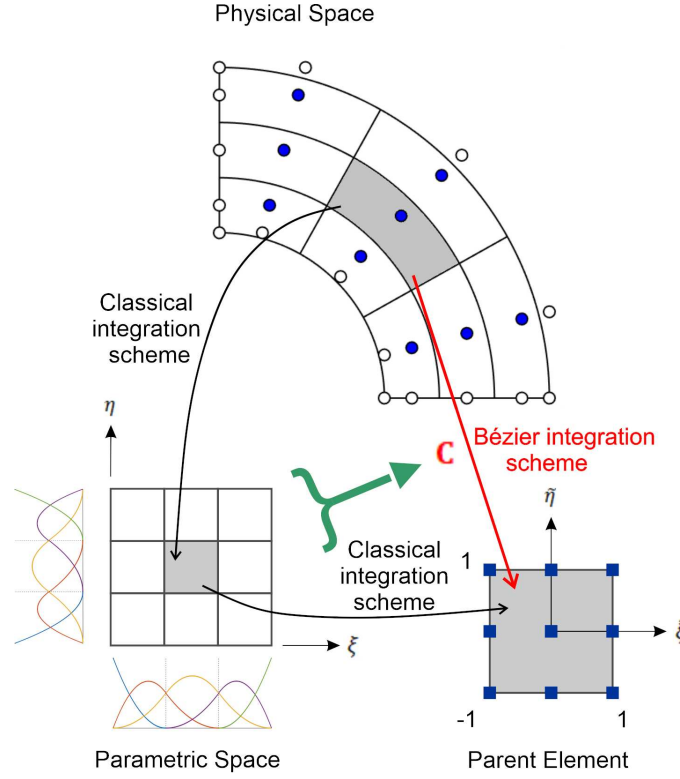


FIGURE 2 Comparison between standard and Bézier integration schemes. **C** indicates the Bézier extraction operator.

In a similar manner, test functions $\delta \mathbf{u}$ and δp are discretised as:

$$\delta \mathbf{u} = \mathbf{R}_u (\delta \hat{\mathbf{u}} + \mathcal{H}_{\Gamma_d} \delta \tilde{\mathbf{u}}), \quad \delta p = \mathbf{R}_p (\delta \hat{p} + \mathcal{H}_{\Gamma_d} \delta \tilde{p}). \quad (25)$$

Employing a backward Euler scheme, $\square = \frac{\square^{t+\Delta t} - \square^t}{\Delta t}$, the discretised format of the equilibrium equations, explicitly evaluated at $t + \Delta t$, becomes

$$\begin{aligned} \mathbf{f}_{\hat{\mathbf{u}}}^{\text{int}, t+\Delta t} &= \mathbf{f}_{\hat{\mathbf{u}}}^{\text{ext}, t+\Delta t} \\ \mathbf{f}_{\tilde{\mathbf{u}}}^{\text{int}, t+\Delta t} &= \mathbf{f}_{\tilde{\mathbf{u}}}^{\text{ext}, t+\Delta t} \\ \mathbf{f}_{\hat{p}}^{\text{int}, t+\Delta t} &= \mathbf{f}_{\hat{p}}^{\text{ext}, t+\Delta t} \\ \mathbf{f}_{\tilde{p}}^{\text{int}, t+\Delta t} &= \mathbf{f}_{\tilde{p}}^{\text{ext}, t+\Delta t} \end{aligned} \quad (26)$$

where the force vectors are given by:

$$\mathbf{f}_{\hat{\mathbf{u}}}^{\text{ext}, t+\Delta t} = \int_{\Gamma_t} \mathbf{R}_u^T \bar{\mathbf{t}} \, d\Gamma \quad (27a)$$

$$\mathbf{f}_{\tilde{\mathbf{u}}}^{\text{ext}, t+\Delta t} = \int_{\Gamma_t} \mathcal{H}_{\Gamma_d} \mathbf{R}_u^T \bar{\mathbf{t}} \, d\Gamma \quad (27b)$$

$$\mathbf{f}_{\hat{p}}^{\text{ext}, t+\Delta t} = \Delta t \int_{\Gamma_q} \mathbf{R}_p^T \mathbf{n}^T \bar{\mathbf{q}} \, d\Gamma \quad (27c)$$

$$\mathbf{f}_{\tilde{p}}^{\text{ext}, t+\Delta t} = \Delta t \int_{\Gamma_q} \mathcal{H}_{\Gamma_d} \mathbf{R}_p^T \bar{\mathbf{q}} \, d\Gamma \quad (27d)$$

$$\mathbf{f}_{\hat{\mathbf{u}}}^{\text{int}, t+\Delta t} = \int_{\Omega} \mathbf{B}_u^T (\boldsymbol{\sigma}_s - \alpha \mathbf{m} (\mathbf{R}_p \hat{\mathbf{p}}^{t+\Delta t} + \mathcal{H}_{\Gamma_d} \mathbf{R}_p \tilde{\mathbf{p}}^{t+\Delta t})) \, d\Omega \quad (28a)$$

$$\mathbf{f}_u^{\text{int}, t+\Delta t} = \int_{\Omega} \mathcal{H}_{\Gamma_d} \mathbf{B}_u^T (\boldsymbol{\sigma}_s - \alpha \mathbf{m} (\mathbf{R}_p \hat{\mathbf{p}}^{t+\Delta t} + \mathcal{H}_{\Gamma_d} \mathbf{R}_p \tilde{\mathbf{p}}^{t+\Delta t})) \, d\Omega + 2 \int_{\Gamma_d} \mathbf{R}_u^T \mathbf{t}_d \, d\Gamma \quad (28b)$$

$$\begin{aligned} \mathbf{f}_p^{\text{int}, t+\Delta t} = & - \int_{\Omega} \alpha \mathbf{R}_p^T \mathbf{m}^T (\mathbf{B}_u \hat{\mathbf{u}}^{t+\Delta t} + \mathcal{H}_{\Gamma_d} \mathbf{B}_u \tilde{\mathbf{u}}^{t+\Delta t}) \, d\Omega - \Delta t \int_{\Omega} k_f \mathbf{B}_p^T (\mathbf{B}_p \hat{\mathbf{p}}^{t+\Delta t} + \mathcal{H}_{\Gamma_d} \mathbf{B}_p \tilde{\mathbf{p}}^{t+\Delta t}) \, d\Omega \\ & - \int_{\Omega} \frac{1}{M} \mathbf{R}_p^T (\mathbf{R}_p \hat{\mathbf{p}}^{t+\Delta t} + \mathcal{H}_{\Gamma_d} \mathbf{R}_p \tilde{\mathbf{p}}^{t+\Delta t}) \, d\Omega + \int_{\Omega} \alpha \mathbf{R}_p^T \mathbf{m}^T (\mathbf{B}_u \hat{\mathbf{u}}^t + \mathcal{H}_{\Gamma_d} \mathbf{B}_u \tilde{\mathbf{u}}^t) \, d\Omega \\ & + \int_{\Omega} \frac{1}{M} \mathbf{R}_p^T (\mathbf{R}_p \hat{\mathbf{p}}^t + \mathcal{H}_{\Gamma_d} \mathbf{R}_p \tilde{\mathbf{p}}^t) \, d\Omega \end{aligned} \quad (28c)$$

$$\begin{aligned} \mathbf{f}_p^{\text{int}, t+\Delta t} = & - \int_{\Omega} \mathcal{H}_{\Gamma_d} \alpha \mathbf{R}_p^T \mathbf{m}^T (\mathbf{B}_u \hat{\mathbf{u}}^{t+\Delta t} + \mathcal{H}_{\Gamma_d} \mathbf{B}_u \tilde{\mathbf{u}}^{t+\Delta t}) \, d\Omega - \Delta t \int_{\Omega} \mathcal{H}_{\Gamma_d} k_f \mathbf{B}_p^T (\mathbf{B}_p \hat{\mathbf{p}}^{t+\Delta t} + \mathcal{H}_{\Gamma_d} \mathbf{B}_p \tilde{\mathbf{p}}^{t+\Delta t}) \, d\Omega \\ & - \int_{\Omega} \mathcal{H}_{\Gamma_d} \frac{1}{M} \mathbf{R}_p^T (\mathbf{R}_p \hat{\mathbf{p}}^{t+\Delta t} + \mathcal{H}_{\Gamma_d} \mathbf{R}_p \tilde{\mathbf{p}}^{t+\Delta t}) \, d\Omega - 2 \int_{\Gamma_d} k_d \mathbf{R}_p^T \mathbf{R}_p \tilde{\mathbf{p}}^{t+\Delta t} \, d\Gamma + \int_{\Omega} \mathcal{H}_{\Gamma_d} \alpha \mathbf{R}_p^T \mathbf{m}^T (\mathbf{B}_u \hat{\mathbf{u}}^t + \mathcal{H}_{\Gamma_d} \mathbf{B}_u \tilde{\mathbf{u}}^t) \, d\Omega \\ & + \int_{\Omega} \mathcal{H}_{\Gamma_d} \frac{1}{M} \mathbf{R}_p^T (\mathbf{R}_p \hat{\mathbf{p}}^t + \mathcal{H}_{\Gamma_d} \mathbf{R}_p \tilde{\mathbf{p}}^t) \, d\Omega \end{aligned} \quad (28d)$$

Using the identity $\int_{\Omega} \delta_{\Gamma_d}(x) \phi(x) \, d\Omega = \int_{\Gamma} \phi(x) \, d\Gamma$ the linearised set of equations for a Newton-Raphson solution method reads:

$$\begin{bmatrix} \mathbf{K}_{\hat{u}\hat{u}}^{\Omega} & \mathbf{K}_{\hat{u}\tilde{u}}^{\Omega} & \mathbf{K}_{\hat{u}\hat{p}}^{\Omega} & \mathbf{K}_{\hat{u}\tilde{p}}^{\Omega} \\ \mathbf{K}_{\tilde{u}\hat{u}}^{\Omega} & \mathbf{K}_{\tilde{u}\tilde{u}}^{\Omega} + \mathbf{K}_{\tilde{u}\tilde{u}}^{\Gamma_d} & \mathbf{K}_{\tilde{u}\hat{p}}^{\Omega} & \mathbf{K}_{\tilde{u}\tilde{p}}^{\Omega} \\ \mathbf{K}_{\hat{p}\hat{u}}^{\Omega} & \mathbf{K}_{\hat{p}\tilde{u}}^{\Omega} & \mathbf{K}_{\hat{p}\hat{p}}^{\Omega} + \mathbf{M}_{\hat{p}\hat{p}}^{\Omega} & \mathbf{K}_{\hat{p}\tilde{p}}^{\Omega} + \mathbf{M}_{\hat{p}\tilde{p}}^{\Omega} \\ \mathbf{K}_{\tilde{p}\hat{u}}^{\Omega} & \mathbf{K}_{\tilde{p}\tilde{u}}^{\Omega} & \mathbf{K}_{\tilde{p}\hat{p}}^{\Omega} + \mathbf{M}_{\tilde{p}\hat{p}}^{\Omega} & \mathbf{K}_{\tilde{p}\tilde{p}}^{\Omega} + \mathbf{M}_{\tilde{p}\tilde{p}}^{\Omega} + \Delta t \frac{\partial \mathbb{Q}_{\Gamma_d}}{\partial \tilde{p}} \end{bmatrix} \begin{bmatrix} \Delta \hat{\mathbf{u}} \\ \Delta \tilde{\mathbf{u}} \\ \Delta \hat{\mathbf{p}} \\ \Delta \tilde{\mathbf{p}} \end{bmatrix} = \begin{bmatrix} \mathbf{f}_u^{\text{ext}, t+\Delta t} \\ \mathbf{f}_u^{\text{ext}, t+\Delta t} \\ \mathbf{f}_p^{\text{ext}, t+\Delta t} \\ \mathbf{f}_p^{\text{ext}, t+\Delta t} \end{bmatrix} - \begin{bmatrix} \mathbf{f}_u^{\text{int}, t+\Delta t} \\ \mathbf{f}_u^{\text{int}, t+\Delta t} \\ \mathbf{f}_p^{\text{int}, t+\Delta t} \\ \mathbf{f}_p^{\text{int}, t+\Delta t} \end{bmatrix} \quad (29)$$

where $\mathbb{Q}_{\Gamma_d} = -2 \int_{\Gamma_d} k_d \delta \tilde{p} \, d\Gamma$ represents the jump term in the flux over the fracture. The individual stiffness terms are given in Appendix A.

5 | IMPLEMENTATION ASPECTS

Different from the enrichment scheme used in the standard finite element method, the interelement overlap of the NURBS basis functions impedes the straightforward enhancement of control points. The reason lies in the $C^{\mathbb{p}}$ -continuity ($\mathbb{p} > 0$) at the element boundaries. This increases with \mathbb{p} -refinement⁶⁶, i.e. continuity elevation.

It is important in fluid-saturated porous media to satisfy the Ladyzhenskaya-Babuška-Brezzi condition^{67,68}, and therefore, to restrict the order of continuity of the solid part to be one higher than that of the interstitial fluid pressure⁶⁹. Moreover, a quadratic (second-order) NURBS is the minimum continuity-order requirement to guarantee a continuous pressure gradient across element boundaries. Herein, we have adopted quartic (C^3) and cubic (C^2) NURBS for the solid and the fluid parts, respectively. Implications of this choice are discussed in the section with the numerical examples.

5.1 | Enhancement of individual control points

The interelement sharing of control points in IGA increases with order elevation. This is a complication when developing a general scheme for elementwise crack propagation in XIGA⁶⁰. It is crucial that a control point at, or in front of the crack tip is not enriched, even it belongs to cracked elements. The front is defined in two ways, by means of the tangential level-set or the elementwise approach, represented in Figure 3. This is further discussed in the ensuing sections, particularly see Figure 5 in Section 5.2.

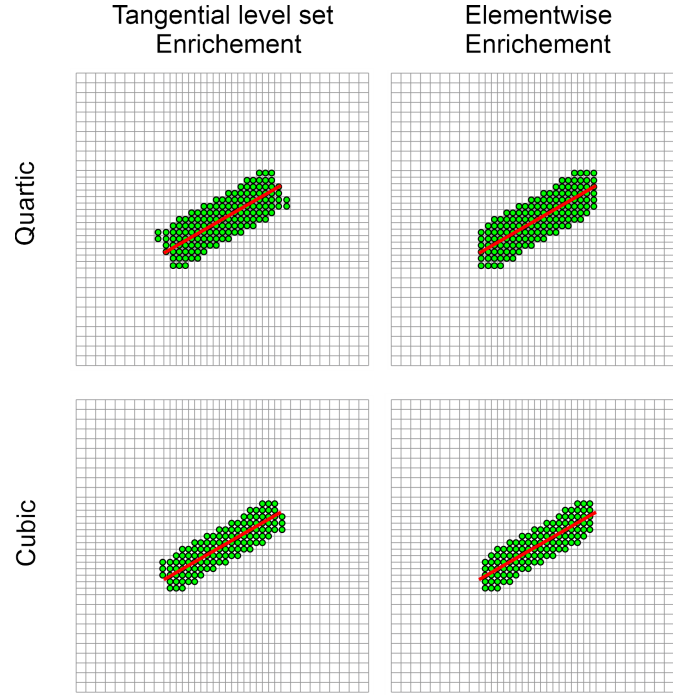


FIGURE 3 Enrichment schemes for quartic and cubic NURBS. Only enriched control points are shown for the sake of clarity.

5.2 | Compatibility enforcement

A proper extended approach preserves the compatibility between the standard and the enhanced fields. For Lagrange basis functions, which provide C^0 -continuity at element boundaries, shifting and blending were adopted to successfully enforce compatibility^{70,71}.

For IGA, however, the interelement share of the control points complicates compatibility enforcement as the control points are not located at element edges. The blending technique has been adopted by De Luycker et al.⁵⁷, while shifting has been studied for XIGA as well⁶⁰, see Figure 4. It was observed that full enforcement of the compatibility between standard and enhanced fields is almost impossible in XIGA. Nevertheless, shifting localises the effect of the enhanced terms to a narrow region perpendicular to the crack path. Therefore, using a fairly fine mesh renders an almost negligible width. Noteworthy is that the XIGA with shifting performs better than XFEM for fine meshes, while XFEM is superior for coarse meshes owing to the full compatibility enforcement⁶¹. Loss of optimal convergence and divergence of the solution are possible consequences of a weak compatibility enforcement for coarse meshes.

Since control points are shared between elements in IGA, domain excess of the enhanced fields occurs, as the tip element shares enriched control points with the element in the front. This causes an unwanted opening of the domain in front of the crack. This can be avoided by adopting a Heaviside step function, see Figure 5. Employing shifting and blending Equations (24-25) become:

$$\dot{\mathbf{u}}(\mathbf{x}) = \sum_{\mathbb{A} \in \mathcal{N}} \mathbf{R}_{u_{\mathbb{A}}}(\mathbf{x}) \dot{\mathbf{u}}_{\mathbb{A}} + \sum_{\mathbb{B} \in \mathcal{N}^H} \mathcal{H}_{\Gamma_d}^{Bl}(\mathbf{x}) \left(\mathcal{H}_{\Gamma_d}^{GP}(\mathbf{x}) - \mathcal{H}_{\Gamma_d}^{\mathbb{B}} \right) \mathbf{R}_{u_{\mathbb{B}}}(\mathbf{x}) \dot{\mathbf{u}}_{\mathbb{B}} \quad (30a)$$

$$p(\mathbf{x}) = \sum_{\mathbb{A} \in \mathcal{N}} \mathbf{R}_{p_{\mathbb{A}}}(\mathbf{x}) \hat{p}_{\mathbb{A}} + \sum_{\mathbb{B} \in \mathcal{N}^H} \mathcal{H}_{\Gamma_d}^{Bl}(\mathbf{x}) \left(\mathcal{H}_{\Gamma_d}^{GP}(\mathbf{x}) - \mathcal{H}_{\Gamma_d}^{\mathbb{B}} \right) \mathbf{R}_{p_{\mathbb{B}}}(\mathbf{x}) \tilde{p}_{\mathbb{B}} \quad (30b)$$

$$\delta \mathbf{u}(\mathbf{x}) = \sum_{\mathbb{A} \in \mathcal{N}} \mathbf{R}_{u_{\mathbb{A}}}(\mathbf{x}) \delta \hat{\mathbf{u}}_{\mathbb{A}} + \sum_{\mathbb{B} \in \mathcal{N}^H} \mathcal{H}_{\Gamma_d}^{Bl}(\mathbf{x}) \left(\mathcal{H}_{\Gamma_d}^{GP}(\mathbf{x}) - \mathcal{H}_{\Gamma_d}^{\mathbb{B}} \right) \mathbf{R}_{u_{\mathbb{B}}}(\mathbf{x}) \delta \tilde{\mathbf{u}}_{\mathbb{B}} \quad (30c)$$

$$\delta p(\mathbf{x}) = \sum_{\mathbb{A} \in \mathcal{N}} \mathbf{R}_{p_{\mathbb{A}}}(\mathbf{x}) \delta \hat{p}_{\mathbb{A}} + \sum_{\mathbb{B} \in \mathcal{N}^H} \mathcal{H}_{\Gamma_d}^{Bl}(\mathbf{x}) \left(\mathcal{H}_{\Gamma_d}^{GP}(\mathbf{x}) - \mathcal{H}_{\Gamma_d}^{\mathbb{B}} \right) \mathbf{R}_{p_{\mathbb{B}}}(\mathbf{x}) \delta \tilde{p}_{\mathbb{B}} \quad (30d)$$

with $\mathcal{N}^H \subset \mathcal{N}$ the subset enriched by the Heaviside sign function. $\mathcal{H}_{\Gamma_d}^{\mathbb{B}}$ and $\mathcal{H}_{\Gamma_d}^{GP}$ denote the values of the Heaviside sign function at the control point \mathbb{B} and the Gauss point under consideration. $\mathcal{H}_{\Gamma_d}^{Bl}$ is the Heaviside step function defined at the Gauss

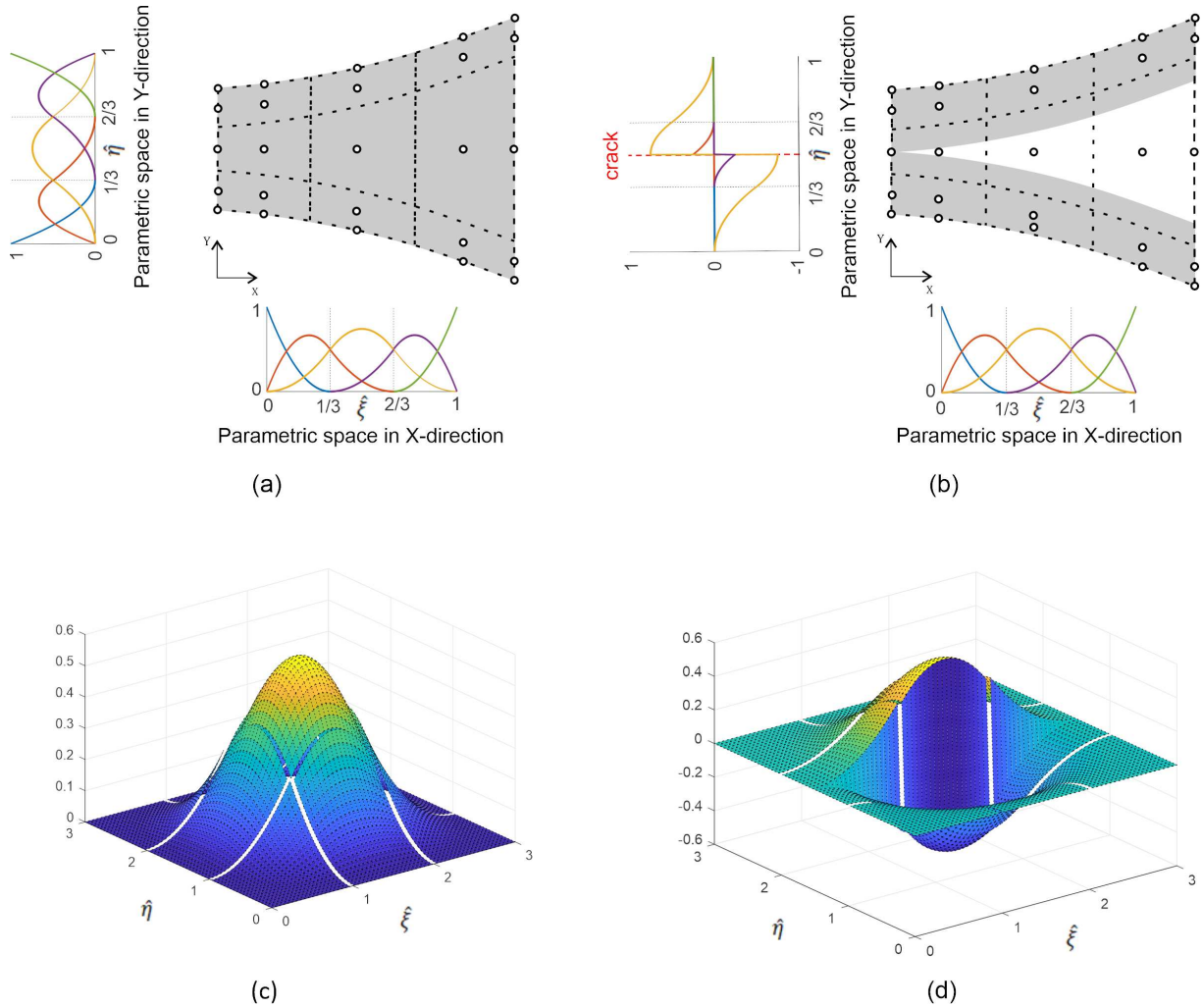


FIGURE 4 Shifted basis functions for quadratic NURBS under mode-I fracture. Univariate NURBS basis functions are shown for intact (a) and shifted discontinuous media (b). The tensor product has been exploited to increase the dimension for bivariate surfaces of intact (c) and shifted discontinuous media (d). Please note that the values at (c) and (d) are illustrated for the control point in the centre of the medium, i.e. tensor product of the yellow curves in (a) and (b).

point with respect to the crack tip⁶⁰. The remaining discretised equations are shifted and blended accordingly, and the Heaviside terms are replaced by the new shifted and blended Heaviside function.

5.3 | Direction of crack extension, integration scheme and point projection

The smoothness of NURBS basis functions provides a better estimate of stresses compared to Lagrange basis functions^{64,21}. Nevertheless, the local stress distribution varies significantly in the vicinity of the crack tip, suggesting a smoothing scheme to be employed. A non-local approach has been adopted here with the Gaussian weight function^{29,36}. Afterwards, the equivalent traction at the extension direction is compared to the fracture strength. Crack nucleation occurs upon satisfying this criterion at certain number of Gauss points along the path⁶⁰.

We have adopted the standard Gauss quadrature for all integration processes in this article. Sub-triangulation have been used to guarantee a sufficient number of Gauss points, evenly distributed at each side of the crack. Making use of the extended approach, a discontinuity is created or extended upon satisfaction of the fracture criterion. This removes the need of a high dummy stiffness used in the interface element approach to avoid undesirable opening prior to fracturing and avoid traction oscillations^{72,53,20}.

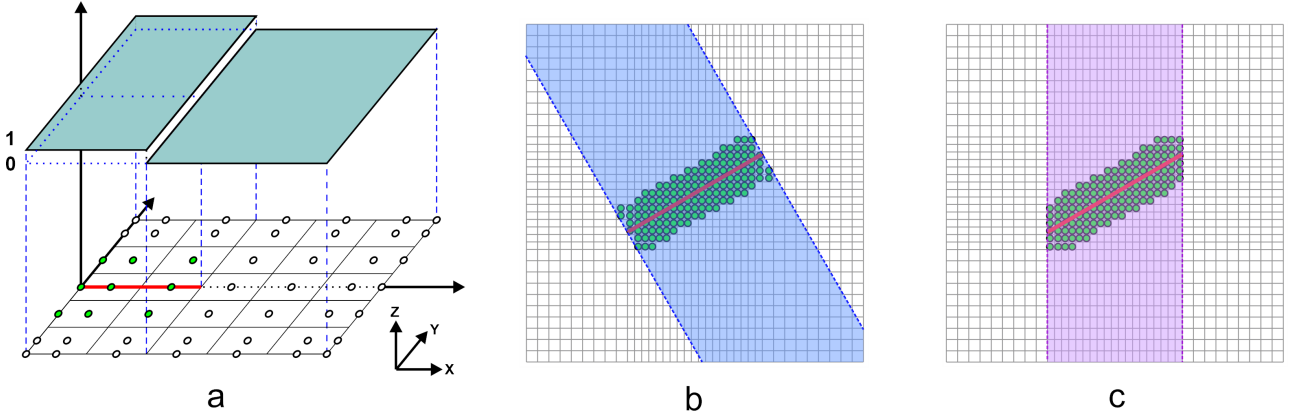


FIGURE 5 Compatibility enforcement in the form of the blending technique. (a) illustrates a Heaviside step function for an edge cracked plate, and active and inactive domains are denoted by 1 and 0, respectively. Enriched control points are designated by green circles, and the red line denotes the crack path. The blending technique is realised by level-set (b) and elementwise (c) enrichments for an inclined crack. The highlighted areas denote the domains where the Heaviside blending function returns 1.

To carry out the line integration for the cohesive tractions a point projection is required⁷³. Since degrees of freedom are not explicitly defined at the discontinuity, the line integration should also be computed in terms of the element degrees of freedom⁶⁰.

6 | NUMERICAL EXAMPLES AND DISCUSSION

We now assess the formulation at the hand of some numerical examples. Different aspects are examined for stationary and fracturing discontinuities comprising straight and curved crack propagation.

6.1 | Stationary cracks: square plate with a centre crack

The first example concerns a stationary crack centred in a square plate, see Figure 6. A plane-strain condition is adopted and the discontinuity is assumed to be traction free. A constant flux $\bar{q} = 10^{-4} \text{ m/s}$ is imposed at the bottom of the plate, while the fluid is allowed to flow freely at the top, see the blue edge in Figure 6. The other boundaries are impermeable. The material properties for the solid are as follows: Young's modulus $E = 9 \text{ GPa}$, Poisson's ratio $\nu = 0.4$, Biot modulus $M = 10^{18} \text{ MPa}$, Biot coefficient $\alpha = 1$, porosity $n_f = 0.3$ and intrinsic permeability $k = 10^{-12} \text{ m}^2$. The fluid viscosity is taken $\mu = 1 \text{ mPa.s}$. The domain is discretised in a non-uniform manner with a refinement in the centre, 37 and 35 elements in the horizontal and the vertical directions, respectively. A time step size $\Delta t = 1 \text{ s}$ has been used until the steady state situation at $t = 40 \text{ s}$. The results are compared with findings from the interface elements³⁷.

6.1.1 | Enrichment scheme

As noted in Section 5.1 two schemes can be adopted for the enrichment: a global scheme based on the tangential level-set and a local scheme based on the tip element. These approaches become virtually indistinguishable for small inclinations, and identical for the limiting case of a horizontal crack. Figure 7 illustrates both enrichment schemes when $\theta = 30^\circ$, see also Figure 3 for quartic and cubic NURBS. A clear difference is observed regarding the enriched control points at the tips of the crack. Regarding the solid part in Figure 7, no enrichment has been employed due to the discontinuous pressure (2PDof) model, where the tangential fluid flow is absent inside the fracture. A similar remedy has been adopted when using interface elements³⁷.

To cover all the enrichment schemes an interface-like enrichment is also adopted here for the limiting case that the crack is on a C^0 -line between elements. Indeed, XIGA can be considered as a generalisation of isogeometric interface elements based on an interelement definition of the discontinuity. As observed from Figure 7 the only drawback of the interface-like enrichment is the need to adapt the crack to the mesh layout. Therefore, it also needs to know the extension path beforehand. On the other

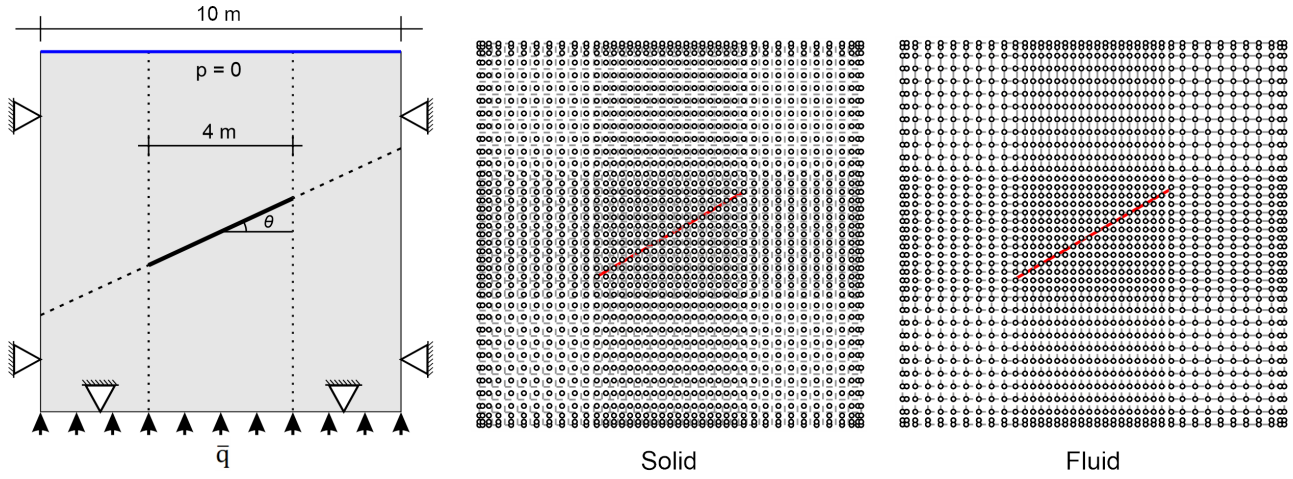


FIGURE 6 Square plate with a centre crack. Discretisations of the solid (quartic) and the fluid (cubic) are shown.

hand, there is no need to enforce compatibility perpendicular to the crack path as the enriched control points in interface-like enrichment only exist on the crack path shared between the cracked elements. Therefore, the shifting technique can be benchmarked against the results of interface-like enrichment perpendicular to the crack path. It is noted that in the tangential direction the blending technique must still be adopted to remove the undesired effect of the enhanced terms ahead of the crack tip(s).

The results are now presented for the three schemes: level-set based, elementwise and interface-like enrichments, rendering nearly identical results in terms of the pressure, see Figure 7. They are also similar to the pressure contours reported by interface element approach³⁷. This agreement is also supported by the pressure diagram along the discontinuity in Figure 8, confirming a good compatibility enforcement by shifting. The figure also includes a comparison with a three degree of freedom pressure (3PDOF) model for the interface³⁷, showing fairly similar results. This gives another confirmation that the present results are in the correct range. Furthermore, the two possible blending domains have been investigated for the interface-like enrichment, where the shifting technique is absent and only the blending technique exists. The results represent an almost identical solution for both of these cases, see Figure 9, suggesting that both enrichments can be adopted for XIGA.

Level-set and elementwise enrichments differ when departing from the horizontal crack. In contrast with the differences observed in the two enrichment schemes in XIGA, compare the enrichments in Figure 3, the results match very well, underscoring the above remark about viability of both suggested enrichment approaches.

6.1.2 | Fracture permeability

To investigate the effect of the interface permeability on the saturated porous media, interstitial fluid pressure and displacement norm are explored for $k_d = k_f$ and $k_d = 0$. The results are similar for level-set and elementwise enrichments, as expected, see Figure 10. The results have also been compared with the findings from 2PDOF standard interface elements in the box in Figure 10³⁷. An excellent agreement is observed.

Finally, the effect of the crack orientation has been investigated for $\theta = 0^\circ$ and 30° in Figure 11. Neither the interstitial fluid pressure nor the displacements 'see' the crack for $k_d = k_f$, as should be. On the contrary, when $k_d = 0$, different patterns in the fluid pressure are observed, as shown in Figure 11. Hence, the fluid pressure makes the displacement field to recognise the presence of the crack, which shows the existence of the solid-fluid interaction.

6.2 | Fracturing: single edge notch test

Straight crack propagation has been examined for a square plate with an edge notch under plane-strain condition, see Figure 12. The notch is assumed traction free, while a cohesive-zone model is used for the fracturing. Therefore the solid as well as the fluid phases are enriched. The simulation is carried out using the following material properties: Young's modulus $E = 25.85$ GPa, Poisson's ratio $\nu = 0.18$, Biot modulus $M = 10^{18}$ MPa, Biot coefficient $\alpha = 1$, porosity $n_f = 0.2$, intrinsic permeability $k = 2.78 \times 10^{-10}$ mm², solid bulk modulus $K_s = 13.46$ GPa, fluid bulk modulus $K_f = 0.2$ GPa, fluid viscosity $\mu = 1$ mPa.s,

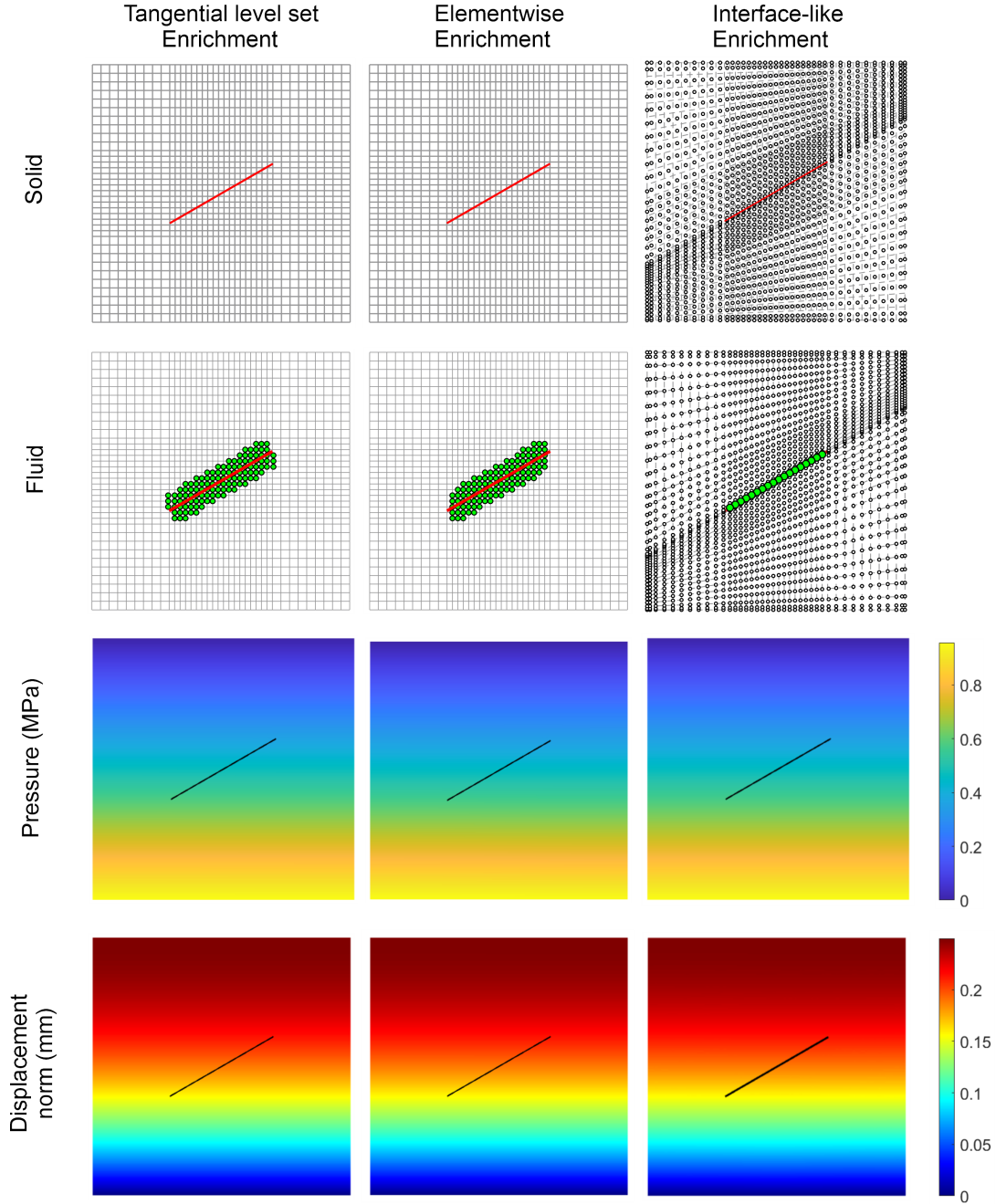


FIGURE 7 Enrichment schemes for the square plate with the centre crack ($\theta = 30^\circ$). No enrichment for solid has been adopted.

fracture energy $G_f = 0.095$ N/mm and fracture strength $f_t = 2.7$ MPa. Vertical velocities $\dot{u} = 2.35 \times 10^{-3}$ mm/s are applied at the top and the bottom of the plate. All boundaries are assumed to be impermeable except for the crack profile whose permeability, k_d , is taken the same as k_f . Two discretisations, 35×35 and 45×45 , are investigated using a quartic-cubic (solid-fluid) NURBS mesh. Similar to Section 6.1, an interface-like enrichment serves as a benchmark to validate the results. It is noted that the level-set and elementwise enrichments render the same results.

The load-displacement diagram in Figure 13 shows an excellent agreement between the discretisations for XIGA and the limiting case of the interface-like enrichment. Moreover, a comparison between the two discretisations is given for the interstitial fluid pressure and the norm of the fluid flux in Figure 14. Again, a close agreement is observed.

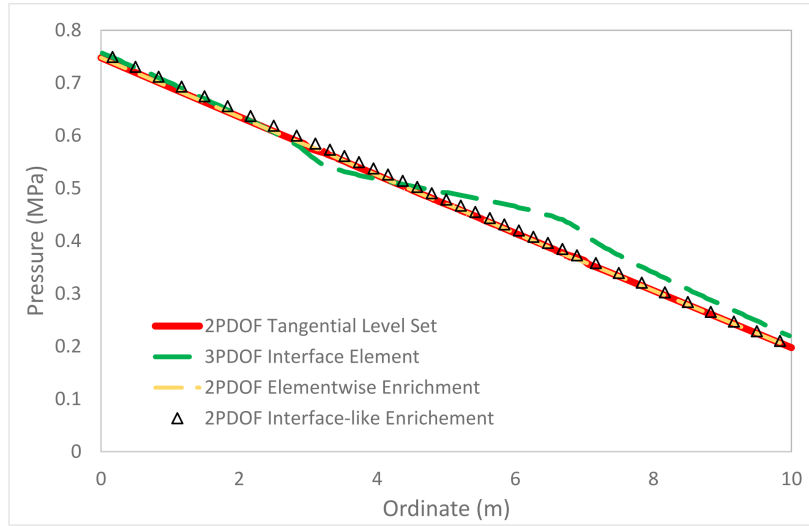


FIGURE 8 Pressure diagram along the crack: level-set based, elementwise and interface-like enrichments are reported. A 3PDOF standard interface element pressure profile³⁷ is also shown for comparison.

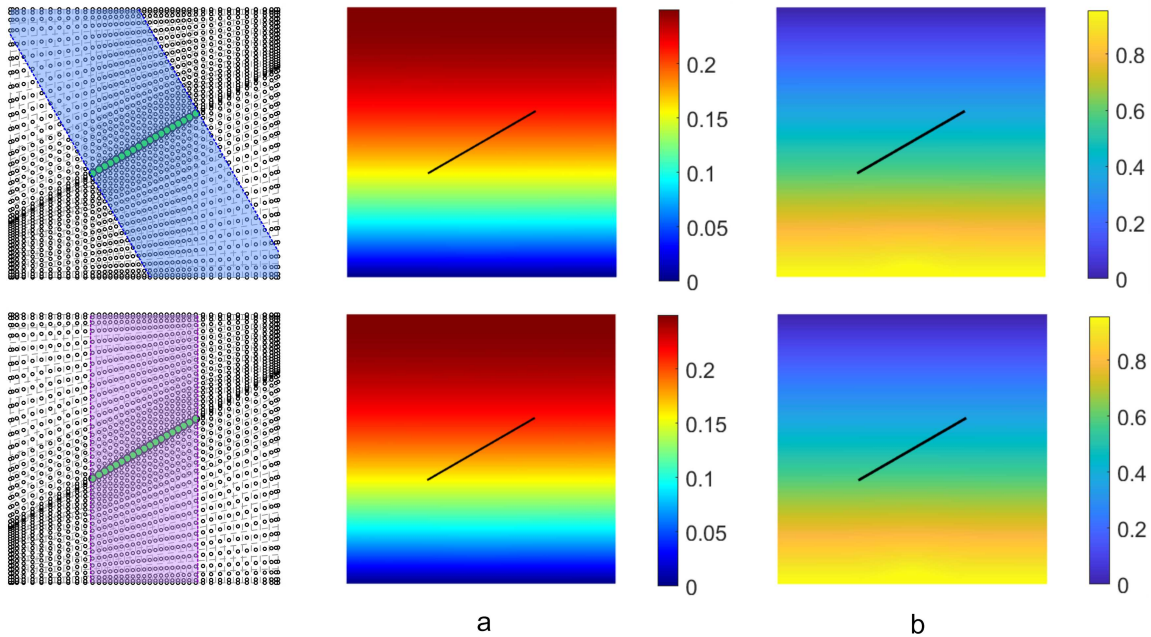


FIGURE 9 Assessment of the blending domain in the form of (a) displacement norm and (b) interstitial fluid pressure contours for interface-like enrichment. The top row denotes the level-set enrichment, while the elementwise enrichment is illustrated in the bottom row.

6.3 | Arbitrary propagation: single edge notch test

Extended approaches have been designed to capture arbitrary crack propagation. To examine this feature for XIGA in the context of fluid-saturated porous media, the single-edge notch test is considered again, Figure 15. The plate is subjected to a horizontal loading $\dot{u} = 0.05$ mm/s at the top. The length of the notch extends to the centre of the plate, and the material properties are as in Section 6.2. Again, all boundaries are assumed to be impermeable except for the crack profile whose permeability, k_d , is taken the same as k_f . In view of the results in the previous sections, only the level-set enrichment is utilised here.

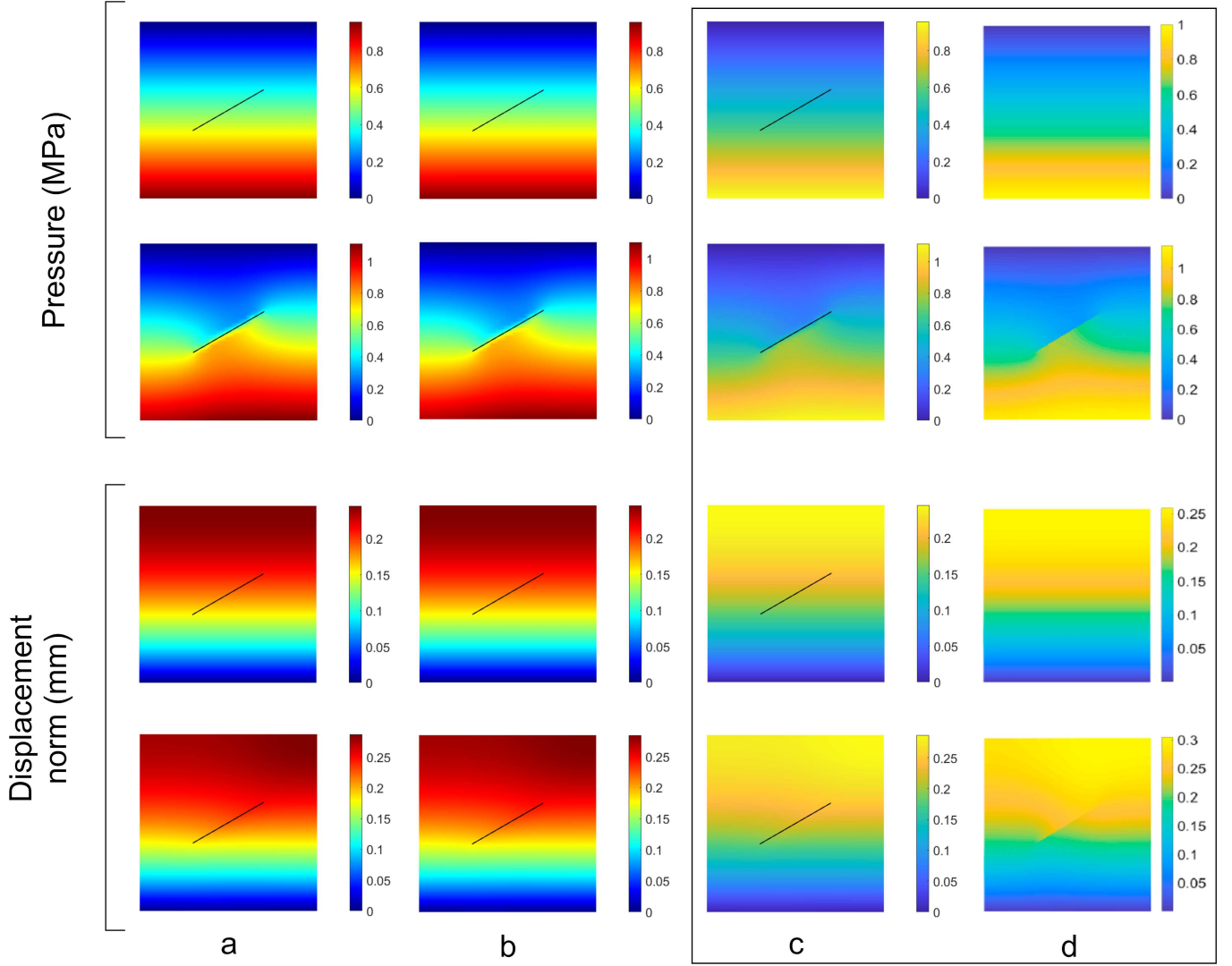


FIGURE 10 Effect of an impervious interface is compared with one with the same permeability of the interstitial fluid, $k_d = k_f$. Odd rows illustrate the permeable interface and even rows denote the impervious interface. (a) indicates the level-set and (b) shows the elementwise enrichment. For visualisation purposes, (c) portrays the column (a) in Parula colormap to compare with the results of the interface element³⁷ in (d).

Two discretisations with the same number of elements, but with a different mesh lay-out, have been considered. The results, in the form of contours of the pressure and the norm of the fluid flux, are illustrated in Figure 16. It is observed that the crack paths and the contour patterns almost coincide. As expected, a smoother contour results due to mesh refinement in the vicinity of the crack tip. This agreement is also shown by the load-displacement diagram in Figure 17.

7 | CONCLUDING REMARKS

An extended isogeometric approach (XIGA) has been developed for fracture simulation in a fluid-saturated porous medium. A cohesive-zone model governs the discontinuity for the solid part, while a two-pressure degrees of freedom (2PDOF) model has been adopted to account for the discontinuity within the pressure. Heaviside sign and step functions have been exploited to enforce compatibility perpendicular and parallel to the crack path in the forms of shifting and blending techniques, respectively. The higher continuity inherent in isogeometric analysis automatically ensures local mass conservation at element boundaries. The lack of such continuity is a deficiency observed in C^0 -continuous elements at their boundaries.

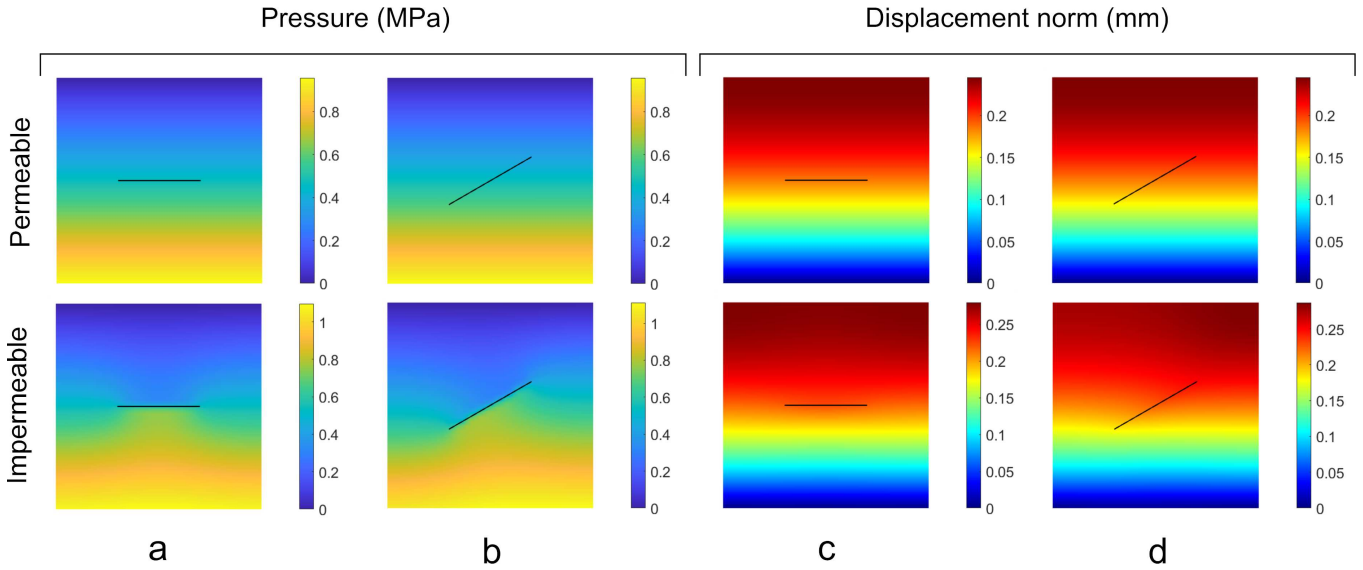


FIGURE 11 Crack orientation for permeable/impermeable fracture. (a) and (b) are $\theta = 0^\circ$ and 30° for the pressure, similar to (c) and (d) for the displacement norm.

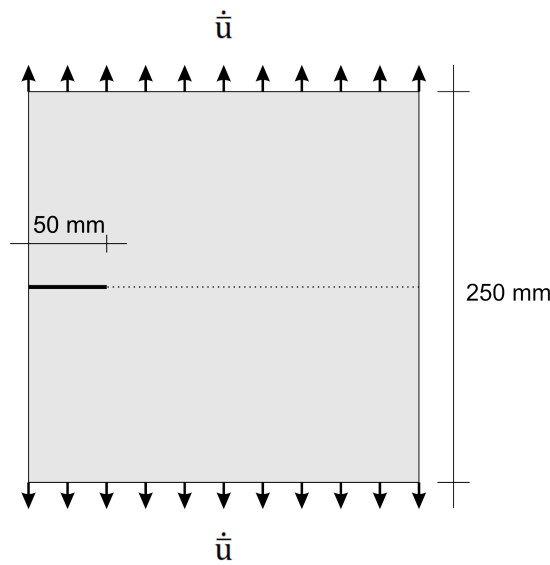


FIGURE 12 Pre-notched square plate subjected to mode-I fracture.

Non-Uniform Rational B-Splines (NURBS) basis functions have been adopted and then cast in the standard finite element data structure using Bézier extraction. The results are compared with findings from interface elements, as well as an interface-like enrichment.

Two types of enrichment have been assessed for XIGA: a global level-set based and a local elementwise enrichment. These approaches yield almost identical results. Moreover, the blending domain corresponding to these two enrichment schemes have been examined for the interface-like enrichment case, where no shifting exists and blending governs the compatibility enforcement. Again, the results are similar, in further support of earlier statements about about enrichment. An excellent agreement has been observed for the stationary crack problem compared to results by interface elements. Proof of the fluid-solid interaction has been observed at the hand of an interface permeability study. Straight and arbitrary fracturing have also been assessed and simulations yield most satisfactory results.

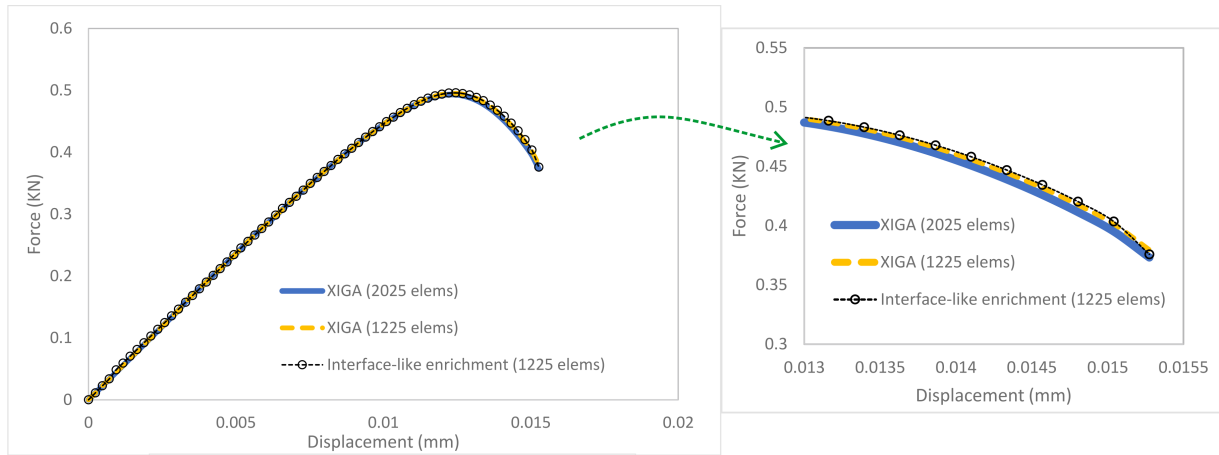


FIGURE 13 Force-displacement diagram for the single-edge notch test.

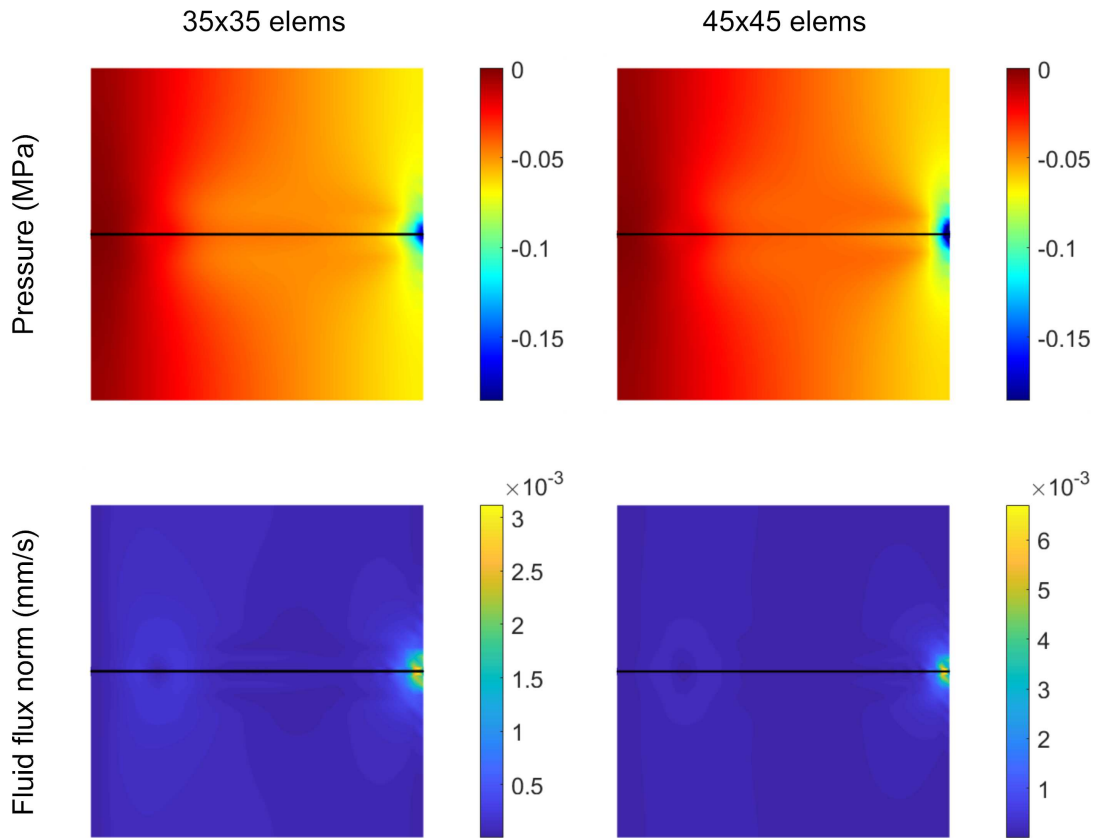


FIGURE 14 Pressure and norm of fluid flux contours for the single-edge notch test.

ACKNOWLEDGMENT

Financial support through H2020 European Research Council Advanced Grant 664734 "PoroFrac" is gratefully acknowledged.

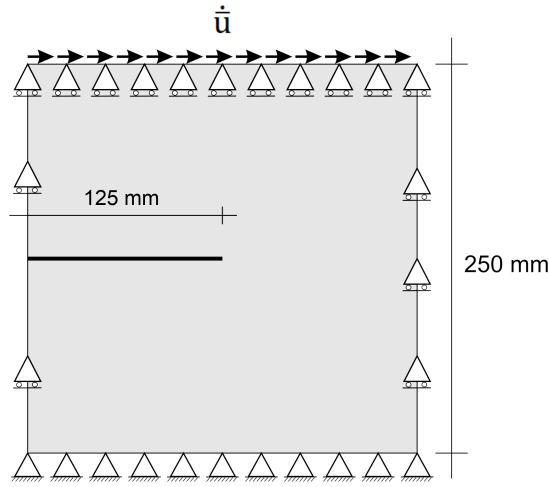


FIGURE 15 Pre-notched square plate subjected to shear loading at the top.

DATA AVAILABILITY STATEMENT

Data sharing is not applicable to this article since no data sets were generated or analysed during this study.

DECLARATION OF CONFLICT OF INTEREST

The authors declare that they have no conflict of interest, and that the research findings reported here have not been published elsewhere or are under review for another publication.

How to cite this article: Fathi F., Chen L., Hageman T. and de Borst R. (2021), Extended isogeometric analysis of a progressively fracturing fluid-saturated porous medium, *Int J Numer Methods Eng.*, 2021.

APPENDIX

A LINEARISED TANGENTIAL STIFFNESS MATRIX

Enriched strain-displacement matrices for a given Gauss point whose global location is indicated by \mathbf{x} read:

$$\mathbf{B}_{u_i}^{\text{enr}} = \mathcal{H}_{\Gamma_d}^{Bl}(\mathbf{x}) \left(\mathcal{H}_{\Gamma_d}^{GP}(\mathbf{x}) - \mathcal{H}_{\Gamma_d}^i \right) \mathbf{B}_{u_i} = \mathcal{H}_{\Gamma_d}^{Bl}(\mathbf{x}) \left(\mathcal{H}_{\Gamma_d}^{GP}(\mathbf{x}) - \mathcal{H}_{\Gamma_d}^i \right) \begin{bmatrix} \frac{\partial R_{u_i}}{\partial X_1} & 0 \\ 0 & \frac{\partial R_{u_i}}{\partial X_2} \\ \frac{\partial R_{u_i}}{\partial X_2} & \frac{\partial R_{u_i}}{\partial X_1} \end{bmatrix} \quad (\text{A1a})$$

$$\mathbf{B}_{p_i}^{\text{enr}} = \mathcal{H}_{\Gamma_d}^{Bl}(\mathbf{x}) \left(\mathcal{H}_{\Gamma_d}^{GP}(\mathbf{x}) - \mathcal{H}_{\Gamma_d}^i \right) \mathbf{B}_{p_i} = \mathcal{H}_{\Gamma_d}^{Bl}(\mathbf{x}) \left(\mathcal{H}_{\Gamma_d}^{GP}(\mathbf{x}) - \mathcal{H}_{\Gamma_d}^i \right) \begin{bmatrix} \frac{\partial R_{p_i}}{\partial X_1} \\ \frac{\partial R_{p_i}}{\partial X_2} \end{bmatrix}. \quad (\text{A1b})$$

Next, the enriched basis functions yield:

$$\mathbf{R}_{u_i}^{\text{enr}} = \mathcal{H}_{\Gamma_d}^{Bl}(\mathbf{x}) \left(\mathcal{H}_{\Gamma_d}^{GP}(\mathbf{x}) - \mathcal{H}_{\Gamma_d}^i \right) \mathbf{R}_{u_i} = \mathcal{H}_{\Gamma_d}^{Bl}(\mathbf{x}) \left(\mathcal{H}_{\Gamma_d}^{GP}(\mathbf{x}) - \mathcal{H}_{\Gamma_d}^i \right) \begin{bmatrix} R_{u_i} & 0 \\ 0 & R_{u_i} \end{bmatrix} \quad (\text{A2a})$$

$$R_{p_i}^{\text{enr}} = \mathcal{H}_{\Gamma_d}^{Bl}(\mathbf{x}) \left(\mathcal{H}_{\Gamma_d}^{GP}(\mathbf{x}) - \mathcal{H}_{\Gamma_d}^i \right) R_{p_i} \quad (\text{A2b})$$

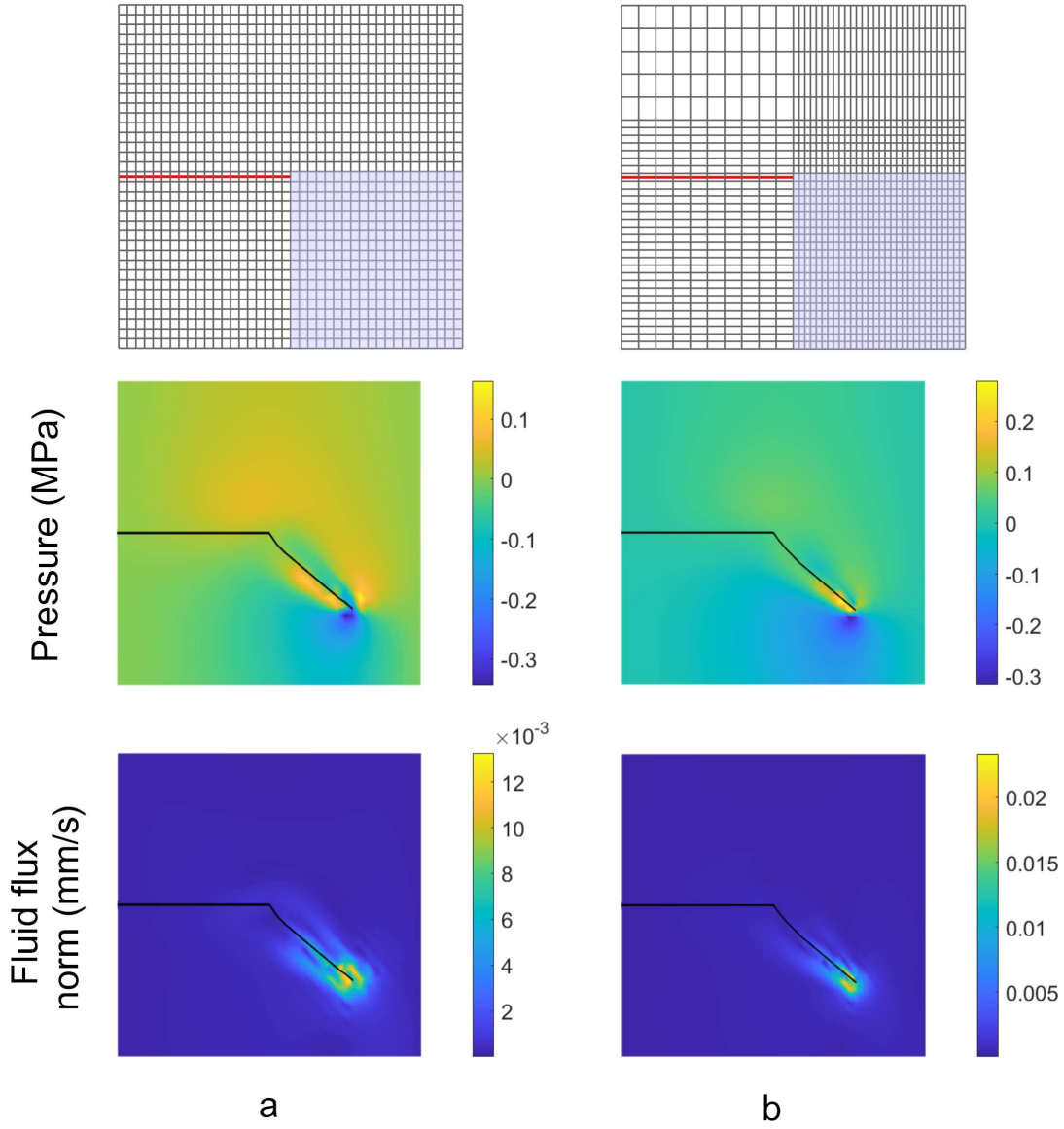


FIGURE 16 Single edge notch test: (a) uniform mesh with 1400 elements (360 elements at the highlighted section): (b) locally refined mesh with 1400 elements (690 elements at the highlighted section). The pressure and fluid flux contours are illustrated for each case.

where X_1 and X_2 denote the global coordinates system, $i = 1, \dots, n_{\text{enr}}$ is the index of the enriched control point, and n_{enr} indicates the total number of the enriched control points within the element under consideration. The tangent terms in Equation (29) read:

$$\mathbf{K}_{\hat{u}\hat{u}}^{\Omega} = \int_{\Omega} \mathbf{B}_u^T \mathbf{D} \mathbf{B}_u d\Omega \quad (\text{A3a})$$

$$\mathbf{K}_{\hat{u}\hat{u}}^{\Omega} = (\mathbf{K}_{\hat{u}\hat{u}}^{\Omega})^T = \int_{\Omega} \mathbf{B}_u^T \mathbf{D} \mathbf{B}_u^{\text{enr}} d\Omega \quad (\text{A3b})$$

$$\mathbf{K}_{\hat{u}\hat{p}}^{\Omega} = (\mathbf{K}_{\hat{p}\hat{u}}^{\Omega})^T = - \int_{\Omega} \alpha \mathbf{B}_u^T \mathbf{m} \mathbf{R}_p d\Omega \quad (\text{A3c})$$

$$\mathbf{K}_{\hat{u}\hat{p}}^{\Omega} = (\mathbf{K}_{\hat{p}\hat{u}}^{\Omega})^T = - \int_{\Omega} \alpha \mathbf{B}_u^T \mathbf{m} \mathbf{R}_p^{\text{enr}} d\Omega \quad (\text{A3d})$$

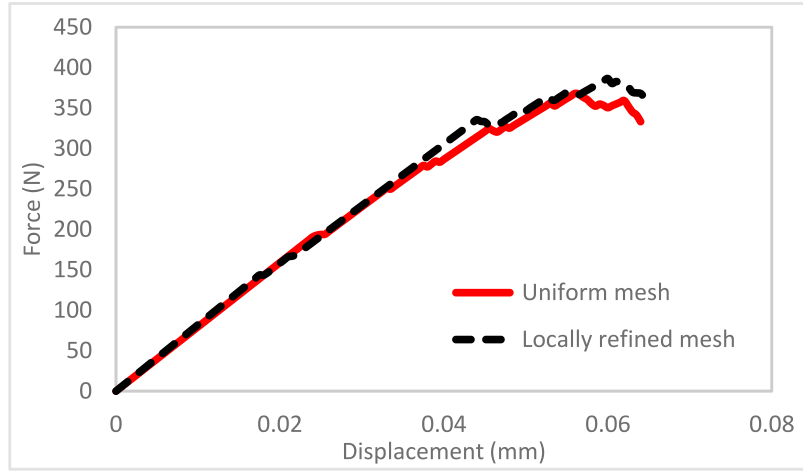


FIGURE 17 Load-displacement diagram for arbitrary propagation in a single edge notch test.

$$\mathbf{K}_{\tilde{u}\tilde{u}}^{\Omega} = \int_{\Omega} (\mathbf{B}_u^{\text{enr}})^T \mathbf{D} \mathbf{B}_u^{\text{enr}} d\Omega \quad (\text{A3e})$$

$$\mathbf{K}_{\tilde{u}\tilde{u}}^{\Gamma_d} = 4 \int_{\Gamma_d} \mathbf{R}_u^T \mathbf{Q}^T \mathbf{T} \mathbf{Q} \mathbf{R}_u d\Gamma \quad (\text{A3f})$$

$$\mathbf{K}_{\tilde{u}\tilde{p}}^{\Omega} = (\mathbf{K}_{\tilde{p}\tilde{u}}^{\Omega})^T = - \int_{\Omega} \alpha (\mathbf{B}_u^{\text{enr}})^T \mathbf{m} \mathbf{R}_p d\Omega \quad (\text{A3g})$$

$$\mathbf{K}_{\tilde{u}\tilde{p}}^{\Omega} = (\mathbf{K}_{\tilde{p}\tilde{u}}^{\Omega})^T = - \int_{\Omega} \alpha (\mathbf{B}_u^{\text{enr}})^T \mathbf{m} \mathbf{R}_p^{\text{enr}} d\Omega \quad (\text{A3h})$$

$$\mathbf{K}_{\tilde{p}\tilde{p}}^{\Omega} = -\Delta t \int_{\Omega} k_f \mathbf{B}_p^T \mathbf{B}_p d\Omega \quad (\text{A3i})$$

$$\mathbf{M}_{\tilde{p}\tilde{p}}^{\Omega} = - \int_{\Omega} \frac{1}{M} \mathbf{R}_p^T \mathbf{R}_p d\Omega \quad (\text{A3j})$$

$$\mathbf{K}_{\tilde{p}\tilde{p}}^{\Omega} = (\mathbf{K}_{\tilde{p}\tilde{p}}^{\Omega})^T = -\Delta t \int_{\Omega} k_f \mathbf{B}_p^T \mathbf{B}_p^{\text{enr}} d\Omega \quad (\text{A3k})$$

$$\mathbf{M}_{\tilde{p}\tilde{p}}^{\Omega} = (\mathbf{M}_{\tilde{p}\tilde{p}}^{\Omega})^T = - \int_{\Omega} \frac{1}{M} \mathbf{R}_p^T \mathbf{R}_p^{\text{enr}} d\Omega \quad (\text{A3l})$$

$$\mathbf{K}_{\tilde{p}\tilde{p}}^{\Omega} = -\Delta t \int_{\Omega} k_d (\mathbf{B}_p^{\text{enr}})^T \mathbf{B}_p^{\text{enr}} d\Omega \quad (\text{A3m})$$

$$\mathbf{M}_{\tilde{p}\tilde{p}}^{\Omega} = - \int_{\Omega} \frac{1}{M} (\mathbf{R}_p^{\text{enr}})^T \mathbf{R}_p^{\text{enr}} d\Omega \quad (\text{A3n})$$

Herein, \mathbf{Q} is the rotation matrix and $\mathbf{T}_d = \partial \mathbf{t}_d / \partial [\mathbf{u}]$ is the linearised tangent stiffness of the traction-relative displacement relation. The tangent term associated with the jump of the fluid flux at the discontinuity completes the discretised formulation presented above:

$$\frac{\partial \mathbf{Q}_{\Gamma_d}}{\partial \tilde{\mathbf{p}}} = -2 \int_{\Gamma_d} k_d \mathbf{R}_p^T \mathbf{R}_p d\Gamma. \quad (\text{A4})$$

\mathbf{Q} denotes the rotation matrix and $\mathbf{T}_d = \partial \mathbf{t}_d / \partial [\mathbf{u}]$ is the linearised tangent stiffness of the traction-relative displacement relation.

References

1. Verruijt A. *Computational Geomechanics*. Dordrecht: Springer Science & Business Media . 1995.
2. Khoei AR, Haghighat E. Extended finite element modeling of deformable porous media with arbitrary interfaces. *Applied Mathematical Modelling* 2011; 35: 5426–5441.
3. Malakpoor K, Kaasschieter EF, Huyghe JM. Mathematical modelling and numerical solution of swelling of cartilaginous tissues. Part I: modelling of incompressible charged porous media. *ESAIM: Mathematical Modelling and Numerical Analysis* 2007; 41: 661–678.
4. Oomens CWJ, van Campen DH, Grootenboer HJ. A mixture approach to the mechanics of skin. *Journal of Biomechanics* 1987; 20: 877–885.
5. Vankan WJ, Huyghe JM, Slaaf DW, et al. Finite-element simulation of blood perfusion in muscle tissue during compression and sustained contraction. *American Journal of Physiology-Heart and Circulatory Physiology* 1997; 273: H1587–H1594.
6. Snijders H, Huyghe JM, Janssen JD. Triphasic finite element model for swelling porous media. *International Journal for Numerical Methods in Fluids* 1995; 20: 1039–1046.
7. Huyghe JM, Janssen JD. Quadriphasic mechanics of swelling incompressible porous media. *International Journal of Engineering Science* 1997; 35: 793–802.
8. Van Loon R, Huyghe JM, Wijlaars MW, Baaijens FPT. 3D FE implementation of an incompressible quadriphasic mixture model. *International Journal for Numerical Methods in Engineering* 2003; 57: 1243–1258.
9. Terzaghi K, Peck RB, Mesri G. *Soil Mechanics in Engineering Practice*. New York: John Wiley & Sons . 1996.
10. Biot MA. *Mechanics of Incremental Deformations*. New York: John Wiley & Sons . 1965.
11. De Boer R. *Theory of Porous Media - Highlights in the Historical Development and Current State*. Berlin - Heidelberg: Springer . 1996.
12. Lewis RW, Lewis RW, Schrefler B. *The Finite Element Method in the Static and Dynamic Deformation and Consolidation of Porous Media*. Chichester: John Wiley & Sons . 1998.
13. Perkins TK, Kern LR. Widths of hydraulic fractures. *Journal of Petroleum Technology* 1961; 13: 937–949.
14. Geertsma J, De Klerk F. A rapid method of predicting width and extent of hydraulically induced fractures. *Journal of Petroleum Technology* 1969; 21: 1571–1581.
15. Nordgren RP. Propagation of a vertical hydraulic fracture. *Society of Petroleum Engineers Journal* 1972; 12: 306–314.
16. Boone TJ, Ingraffea AR. A numerical procedure for simulation of hydraulically-driven fracture propagation in poroelastic media. *International Journal for Numerical and Analytical Methods in Geomechanics* 1990; 14: 27–47.
17. Schellekens JCJ, de Borst R. On the numerical integration of interface elements. *International Journal for Numerical Methods in Engineering* 1993; 36: 43–66.
18. Segura JM, Carol I. On zero-thickness interface elements for diffusion problems. *International Journal for Numerical and Analytical Methods in Geomechanics* 2004; 28: 947–962.
19. Segura JM, Carol I. Coupled HM analysis using zero-thickness interface elements with double nodes. Part I: Theoretical model. *International Journal for Numerical and Analytical Methods in Geomechanics* 2008; 32: 2083–2101.
20. Irzal F, Remmers JJC, Verhoosel CV, de Borst R. An isogeometric analysis Bézier interface element for mechanical and poromechanical fracture problems. *International Journal for Numerical Methods in Engineering* 2014; 97: 608–628.
21. Vignollet J, May S, de Borst R. Isogeometric analysis of fluid-saturated porous media including flow in the cracks. *International Journal for Numerical Methods in Engineering* 2016; 108: 990–1006.

22. Chen L, Lingen EJ, de Borst R. Adaptive hierarchical refinement of NURBS in cohesive fracture analysis. *International Journal for Numerical Methods in Engineering* 2017; 112: 2151–2173.
23. Chen L, Verhoosel CV, de Borst R. Discrete fracture analysis using locally refined T-splines. *International Journal for Numerical Methods in Engineering* 2018; 116: 117–140.
24. Chen L, de Borst R. Cohesive fracture analysis using Powell-Sabin B-splines. *International Journal for Numerical and Analytical Methods in Geomechanics* 2019; 43: 625–640.
25. Schrefler BA, Secchi S, Simoni L. On adaptive refinement techniques in multi-field problems including cohesive fracture. *Computer Methods in Applied Mechanics and Engineering* 2006; 195: 444–461.
26. Secchi S, Simoni L, A. Schrefler B. Mesh adaptation and transfer schemes for discrete fracture propagation in porous materials. *International Journal for Numerical and Analytical Methods in Geomechanics* 2007; 31: 331–345.
27. Belytschko T, Black T. Elastic crack growth in finite elements with minimal remeshing. *International journal for numerical methods in engineering* 1999; 45: 601–620.
28. Belytschko T, Moës N, Usui S, Parimi C. Arbitrary discontinuities in finite elements. *International Journal for Numerical Methods in Engineering* 2001; 50: 993–1013.
29. Wells GN, Sluys LJ. A new method for modelling cohesive cracks using finite elements. *International Journal for Numerical Methods in Engineering* 2001; 50: 2667–2682.
30. Moës N, Belytschko T. Extended finite element method for cohesive crack growth. *Engineering Fracture Mechanics* 2002; 69: 813–833.
31. Remmers JJC, de Borst R, Needleman A. A cohesive segments method for the simulation of crack growth. *Computational Mechanics* 2003; 31: 69–77.
32. de Borst R, Réthoré J, Abellan MA. A numerical approach for arbitrary cracks in a fluid-saturated medium. *Archive of Applied Mechanics* 2006; 75: 595–606.
33. Réthoré J, de Borst R, Abellan MA. A two-scale approach for fluid flow in fractured porous media. *International Journal for Numerical Methods in Engineering* 2007; 71: 780–800.
34. Réthoré J, de Borst R, Abellan MA. A two-scale model for fluid flow in an unsaturated porous medium with cohesive cracks. *Computational Mechanics* 2008; 42: 227–238.
35. Réthoré J, de Borst R, Abellan MA. A discrete model for the dynamic propagation of shear bands in a fluid-saturated medium. *International Journal for Numerical and Analytical Methods in Geomechanics* 2007; 31: 347–370.
36. Irzal F, Remmers JJC, Huyghe JM, de Borst R. A large deformation formulation for fluid flow in a progressively fracturing porous material. *Computer Methods in Applied Mechanics and Engineering* 2013; 256: 29–37.
37. Fathima KMP, de Borst R. Implications of single or multiple pressure degrees of freedom at fractures in fluid-saturated porous media. *Engineering Fracture Mechanics* 2019; 213: 1–20.
38. Armero F, Callari C. An analysis of strong discontinuities in a saturated poro-plastic solid. *International Journal for Numerical Methods in Engineering* 1999; 46: 1673–1698.
39. Callari C, Armero F. Analysis and numerical simulation of strong discontinuities in finite strain poroplasticity. *Computer Methods in Applied Mechanics and Engineering* 2004; 193: 2941–2986.
40. de Borst R, Remmers JJC, Needleman A, Abellan MA. Discrete vs smeared crack models for concrete fracture: bridging the gap. *International Journal for Numerical and Analytical Methods in Geomechanics* 2004; 28: 583–607.
41. Malakpoor K, Kaasschieter EF, Huyghe JM. Mathematical modelling and numerical solution of swelling of cartilaginous tissues. Part II: Mixed-hybrid finite element solution. *ESAIM: Mathematical Modelling and Numerical Analysis* 2007; 41: 679–712.

42. Rabczuk T, Zi G. A meshfree method based on the local partition of unity for cohesive cracks. *Computational Mechanics* 2007; 39: 743–760.
43. Goudarzi M, Mohammadi S. Analysis of cohesive cracking in saturated porous media using an extrinsically enriched EFG method. *Computers and Geotechnics* 2015; 63: 183–198.
44. Goudarzi M, Mohammadi S. Weak discontinuity in porous media: an enriched EFG method for fully coupled layered porous media. *International Journal for Numerical and Analytical Methods in Geomechanics* 2014; 38: 1792–1822.
45. Hughes TJR, Cottrell JA, Bazilevs Y. Isogeometric analysis: CAD, finite elements, NURBS, exact geometry and mesh refinement. *Computer Methods in Applied Mechanics and Engineering* 2005; 194: 4135–4195.
46. Kagan P, Fischer A, Bar-Yoseph PZ. New B-Spline finite element approach for geometrical design and mechanical analysis. *International Journal for Numerical Methods in Engineering* 1998; 41: 435–458.
47. Kagan P, Fischer A. Integrated mechanically based CAE system using B-Spline finite elements. *Computer-Aided Design* 2000; 32: 539–552.
48. Irzal F, Remmers JJC, Verhoosel CV, de Borst R. Isogeometric finite element analysis of poroelasticity. *International Journal for Numerical and Analytical Methods in Geomechanics* 2013; 37: 1891–1907.
49. de Borst R. *Computational Methods for Fracture in Porous Media: Isogeometric and Extended Finite Element Methods*. New York: Elsevier . 2017.
50. de Borst R. Fluid flow in fractured and fracturing porous media: A unified view. *Mechanics Research Communications* 2017; 80: 47–57.
51. Hageman T, de Borst R. A convergence study of monolithic simulations of flow and deformation in fractured poroelastic media. *International Journal for Numerical Methods in Engineering* 2020; 121: 393–410.
52. Hageman T, de Borst R. Flow of non-Newtonian fluids in fractured porous media: Isogeometric vs standard finite element discretisation. *International Journal for Numerical and Analytical Methods in Geomechanics* 2019; 43: 2020–2037.
53. Hageman T, Fathima KMP, de Borst R. Isogeometric analysis of fracture propagation in saturated porous media due to a pressurised non-Newtonian fluid. *Computers and Geotechnics* 2019; 112: 272–283.
54. Hageman T, de Borst R. A refined two-scale model for Newtonian and non-Newtonian fluids in fractured poroelastic media. *Journal of Computational Physics* 2021; 441: 110424.
55. Hageman T, de Borst R. Sub-grid models for multiphase fluid flow inside fractures in poroelastic media. *Journal of Computational Physics* 2020; 414: 109481.
56. Morganti S, Callari C, Auricchio F, Reali A. Mixed isogeometric collocation methods for the simulation of poromechanics problems in 1D. *Meccanica* 2018; 53(6): 1441–1454.
57. De Luycker E, Benson DJ, Belytschko T, Bazilevs Y, Hsu MC. X-FEM in isogeometric analysis for linear fracture mechanics. *International Journal for Numerical Methods in Engineering* 2011; 87: 541–565.
58. Ghorashi SS, Valizadeh N, Mohammadi S. Extended isogeometric analysis for simulation of stationary and propagating cracks. *International Journal for Numerical Methods in Engineering* 2012; 89: 1069–1101.
59. Nguyen-Thanh N, Valizadeh N, Nguyen MN, et al. An extended isogeometric thin shell analysis based on Kirchhoff-Love theory. *Computer Methods in Applied Mechanics and Engineering* 2015; 284: 265–291.
60. Fathi F, Chen L, de Borst R. Extended isogeometric analysis for cohesive fracture. *International Journal for Numerical Methods in Engineering* 2020; 121: 4584–4613.
61. Fathi F, de Borst R. Geometrically nonlinear extended isogeometric analysis for cohesive fracture with applications to delamination in composites. *Finite Elements in Analysis and Design* 2021; 191: 103527.

62. Fathi F, Chen L, de Borst R. X-IGALME: Isogeometric analysis extended with local maximum entropy for fracture analysis. *International Journal for Numerical Methods in Engineering* 2021. doi: 10.1002/nme.6784
63. Zhang Q, Babuška I, Banerjee U. Robustness in stable generalized finite element methods (SGFEM) applied to Poisson problems with crack singularities. *Computer Methods in Applied Mechanics and Engineering* 2016; 311: 476–502.
64. Borden MJ, Scott MA, Evans JA, Hughes TJR. Isogeometric finite element data structures based on Bézier extraction of NURBS. *International Journal for Numerical Methods in Engineering* 2011; 87: 15–47.
65. de Borst R, Chen L. The role of Bézier extraction in adaptive isogeometric analysis: Local refinement and hierarchical refinement. *International Journal for Numerical Methods in Engineering* 2018; 113: 999–1019.
66. Thomas DC, Scott MA, Evans JA, Tew K, Evans EJ. Bézier projection: a unified approach for local projection and quadrature-free refinement and coarsening of NURBS and T-splines with particular application to isogeometric design and analysis. *Computer Methods in Applied Mechanics and Engineering* 2015; 284: 55–105.
67. Brezzi F, Fortin M. *Mixed and Hybrid Finite Element Methods*. Berlin - Heidelberg: Springer Verlag . 1991.
68. Chapelle D, Bathe KJ. The inf-sup test. *Computers & Structures* 1993; 47: 537–545.
69. Sandhu RS, Liu H, Singh KJ. Numerical performance of some finite element schemes for analysis of seepage in porous elastic media. *International Journal for Numerical and Analytical Methods in Geomechanics* 1977; 1: 177–194.
70. Khoei AR. *Extended Finite Element Method: Theory and Applications*. Chichester: John Wiley & Sons . 2014.
71. Mohammadi S. *XFEM: Fracture Analysis of Composites*. Chichester: John Wiley & Sons . 2008.
72. Vignollet J, May S, de Borst R. On the numerical integration of isogeometric interface elements. *International Journal for Numerical Methods in Engineering* 2015; 102: 1733–1749.
73. Piegl L, Tiller W. *The NURBS Book*. Berlin - Heidelberg: Springer Science & Business Media . 1996.